ACS OMEGA

Open Access

http://pubs.acs.org/journal/acsodf

Mini-Review

Lead-Free Mixed-Halide-Based Vacancy-Ordered Perovskites: Status and Opportunities in Optoelectronics

Walagedara G. A. Pabasara and Galhenage A. Sewvandi*

Cite This: *ACS Omega* 2026, 11, 30219−30235

Read Online

ACCESS | Metrics & More | Article Recommendations

ABSTRACT: Lead halide perovskites have delivered excellent efficiencies in optoelectronic devices owing to their strong light absorption and low-cost fabrication processes. However, toxicity and limited operational stability remain major obstacles to mass-scale commercialization. In this context, vacancy-ordered perovskites (VOPs) based on Bi^{3+}/Sb^{3+}, typically within the $A_3B_2X_9$ structure family, have appeared as promising lead-free alternatives with improved chemical robustness and an attractive optical response. Importantly, their optoelectronic properties are highly tunable through compositional modifications, particularly mixed-halide alloying. Halide substitution (Cl/Br/I) not only permits systematic bandgap and band-edge tuning but can also drive structural and dimensionality transformations (e.g., 0D/1D to 2D layered networks) that improve the electronic connectivity and charge transport. This mini-review consolidates recent progress on lead-free mixed-halide VOPs, demonstrating how halide-driven dimensionality control, site-selective halide ordering, and defect chemistry collectively govern optical transitions, carrier dynamics, and device performance. The mini-review also summarizes key synthesis and thin-film fabrication routes and assesses long-term device stability under relevant stressors. Finally, this mini-review also highlights future opportunities in the phase-pure film growth, the halide homogeneity control, the defect passivation, and the interface/band alignment for the performance enhancement to accelerate the deployment of mixed-halide VOPs across photovoltaics, photodetectors, and emerging optoelectronic platforms.

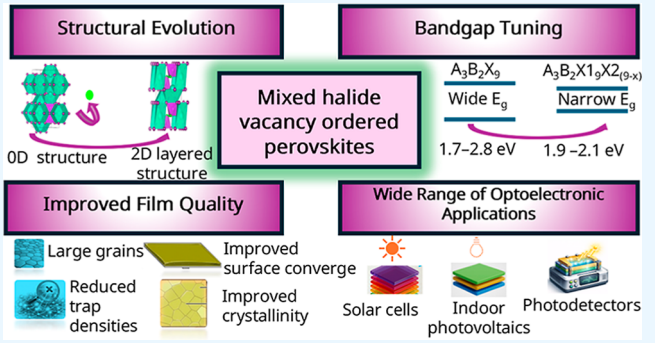

1. INTRODUCTION

Perovskites are leading semiconductor materials that are gaining significant attention over the years in optoelectronic applications.[1] The Pb presence in the high-performance optoelectronic devices is a major drawback that hinders their commercialization.[2−4] Among the different strategies proposed as lead replacement, the vacancy-ordered perovskites (VOPs) are the topmost candidates.[5,6] VOPs are represented by $A_3B_2X_9$ family (A = Cs^+, Rb^+; B = Bi^{3+} or Sb^{3+}; X = $Cl^-/Br^-/I^-$) and their charge neutrality is achieved through an ordered distribution of B-site vacancies, producing BX_6 octahedra that assemble either as isolated $[B_2X_9]^{3-}$ dimers (0D, commonly $P6_3/mmc$) or as (111)-stacked bilayers (2D, commonly $\bar{P}3m1$).[7,8]

Particularly, Bi/Sb-based halide perovskites demonstrate better intrinsic material stability and are excellent light absorbers.[5] Currently, the power conversion efficiency (PCE) of this Bi/Sb-based halide perovskite lies far behind that of the Pb-based ones. However, further improvement of the optoelectronic properties in these Bi/Sb-based halide perovskites can be achieved by introducing structural distortion via the intuitive substitution of suitable elements at various sites. Mixed-halide compositional engineering provides a direct route to tailor optoelectronic properties and, in many cases, overcomes efficiency-related limitations. Substituting smaller halides (Cl^- and Br^-) into I-rich lattices contracts the framework, modifies octahedral tilting, and can drive a dimensional expansion from 0D dimers to 2D layered networks (for example, $Cs_3Bi_2I_9$ to $Cs_3Bi_2I_6Cl_3$ and $Cs_3Sb_2I_9$ to $Cs_3Sb_2Cl_xI_{9-x}$).[8,9] Not limited to bandgap shifts, halide alloying can produce site-selective halide ordering, where I preferentially occupy capping (terminal) positions, while Cl stabilizes bridging sites.[8] Consequently, reordering can promote more direct transitions without large changes in the absorption onset when the band edges remain dominated by I p states and Bi/Sb p states.[8−10] In addition, Br/Cl incorporation can improve phase stability and thin-film morphology, although it also introduces new questions about

Received: February 10, 2026
Revised: May 7, 2026
Accepted: May 11, 2026
Published: May 18, 2026

https://doi.org/10.1021/acsomega.6c01559
ACS Omega 2026, 11, 30219−30235

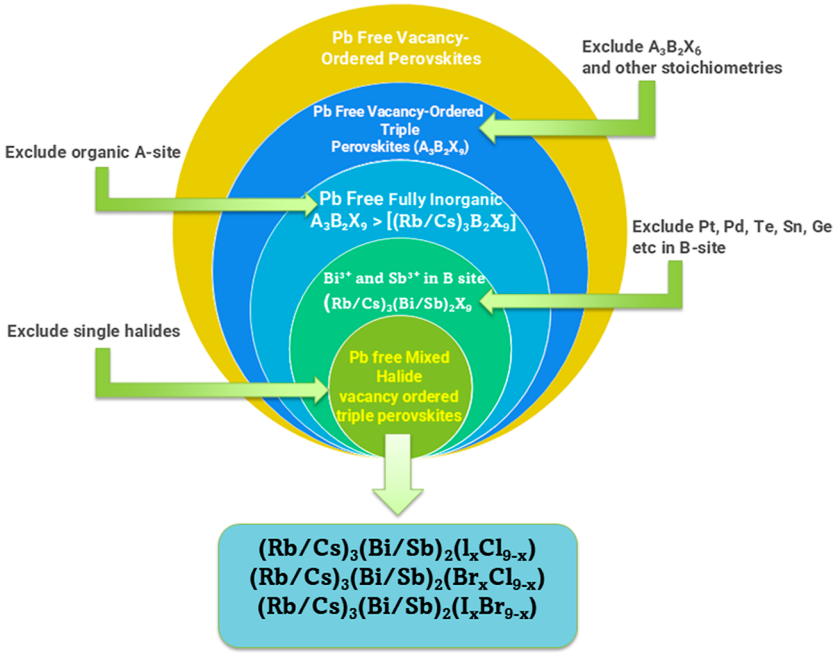

Figure 1. Schematic illustration of the criteria used to select A and B sites in mixed-halide vacancy-ordered $A_3B_2X_9$ systems.

halide homogeneity, defect chemistry, and long-term operational aging.

Several review articles have previously summarized the development of lead-free perovskites and vacancy-ordered halide materials, primarily focusing on broad classes of Pb-free perovskites or vacancy-ordered double perovskites with the general formula A_2BX_6, with particular emphasis on synthesis strategies, structural characteristics, and photovoltaic device architectures.[11,12] However, a focused discussion on mixed-halide vacancy-ordered $A_3B_2X_9$ systems and the mechanisms governing their optoelectronic behavior remains limited. In this context, the present mini review, mixed-halide VOPs with A = Cs^+ or Rb^+ and B = Bi^{3+} or Sb^{3+} are mainly investigated (as shown in Figure 1), as these compositions consist of the most extensively studied and structurally stable lead-free $A_3B_2X_9$ systems. Alkali A-site cations stabilize the inorganic lattice and improve environmental stability, while Bi^{3+} and Sb^{3+} act as effective Pb^{2+} substitutes due to their ns^2 electronic configuration and ability to form BX_6 octahedral frameworks.[1,8] As a result, Cs/Rb−Bi/Sb systems dominate the current literature on VOPs and provide the most representative platform for exploring halide-alloying effects and their influence on optoelectronic performances. By linking these structural mechanisms to optoelectronic metrics and device-level outcomes across photovoltaics, photodetection, and emerging self-powered platforms, and by summarizing synthesis techniques that govern phase purity and halide homogeneity, the review delivers a targeted roadmap that complements broader Bi/Sb perovskite-inspired material surveys.

2. STRUCTURAL AND OPTOELECTRONIC PROPERTIES OF MIXED-HALIDE VOPS

2.1. Structural Properties of Mixed-Halide VOPs

VOPs are derived from the ABX_3 lattice by replacing B-site cations with trivalent metal cations such as Bi^{3+} and Sb^{3+}. This substitution yields corner-sharing BX_6 octahedra that assemble as isolated $[B_2X_9]^{3-}$ dimers (0D, $P6_3/mmc$) or (111)-stacked bilayers (2D, $\bar{P}3m1$). Mixed-halide substitution (Cl/Br/I) tunes topology and modulates the strength of interdimer or interlayer coupling.

I-rich compositions due to the larger ionic radii, more polarizable nature of I^-, favor the 0D dimer motif; introducing Cl^-/Br^- contracts the lattice and strengthens interoctahedral bonding, frequently driving a 0D to 2D transition (e.g., 0D-$Cs_3Sb_2I_9$ into 2D-$Cs_3Sb_2Cl_xI_{9-x}$ and 0D-$Cs_3Bi_2I_9$ into 2D-$Cs_3Bi_2I_6Cl_3$). The 2D phase raises electronic dimensionality and often converts indirect-like optical edges toward the direct-gap behavior.[8,13] When considering the site selectivity of the substitution atom, in-layered 2D-$Cs_3Bi_2I_6Cl_3$ mixed-halide VOPs, the octahedra comprise three capping I atoms that terminate the layers and three bridging Cl atoms that connect to octahedra in the opposite layer. This ordering arises due to a larger size mismatch between Cl (ionic radius 1.81 Å) and I (ionic radius 2.20 Å).[8] Sara Bonami et al. proved that, as Br content increases in $Cs_3Bi_2(I_{1-x}Br_x)_9$, the structure progressively transforms from the I-rich framework into the trigonal $\bar{P}3m1$ Br-rich phase, passing through a mixed-phase regime marked by broadened, blue-shifting Bi−I Raman modes and the emergence of Br-sensitive features, while the lattice contracts and the optical edge blue-shifts accordingly.[6]

In conclusion, mixed-halide VOPs exhibit composition-dependent structural and electronic tunability, where varying halide contents control lattice dimensionality, symmetry, and bonding. It enables precise modulation of their optoelectronic and structural stability properties for advanced, lead-free photovoltaic and photonic applications.

2.2. Bandgap Tuning of Mixed-Halide VOPs

Mixed-halide vacancy-ordered perovskites (VOPs) exhibit tunable band gaps and optoelectronic responses strongly dependent on halide composition and structural dimensionality. Iodine-rich compounds, such as $Cs_3Bi_2I_9$, show indirect band gaps around 2.2 eV, associated with their 0D dimeric structure. Introducing smaller halides like Cl^- or Br^- contracts

https://doi.org/10.1021/acsomega.6c01559
ACS Omega 2026, 11, 30219−30235

the lattice, increases orbital overlap, and promotes 2D connectivity, thus leading to direct-gap behavior and adjustable optical absorption. For example, $Cs_3Bi_2I_6Cl_3$ has a direct band gap of 2.05 eV, while $Cs_3Bi_2Br_3I_6$ exhibits a direct band gap of 2.05 eV.[8] The $Rb_3Bi_2I_6Cl_3$ and $Rb_3Bi_2I_3Cl_6$ halide perovskites exhibit narrow, direct−indirect band gaps suitable for visible-light optoelectronic applications. Density functional theory (DFT) calculations show that $Rb_3Bi_2I_6Cl_3$ possesses a direct bandgap of 2.061 eV and an indirect gap of 2.051 eV, while $Rb_3Bi_2I_3Cl_6$ shows nearly degenerate direct and indirect band gaps of 1.996 eV at the same symmetry points.[10] Experimentally, $Rb_3Bi_2I_6Cl_3$ exhibits a bandgap of nearly 2.02 eV, in excellent agreement with theoretical predictions. Giovilli reported that $Cs_3Sb_2Br_{9-x}I_x$ mixed-halide perovskites show a tunable bandgap ranging from 2.5 eV for Br-rich compositions to about 1.95 eV for I-rich ones. The study further showed a relevant initial reduction of the (direct) band gap from about 2.5 to 2.1 eV (at 50% of Br and I), followed by a smoother reduction of the band gap up to about 2.0 eV, showing a bowing of the band gap.[14]

3. PROGRESS IN MIXED-HALIDE VOPS

3.1. Cs-Based VOPs

3.1.1. Bi-Based Cl/I Mixed-Halide Systems. Cs-based mixed-halide VOPs can be mainly categorized into two classes, Bi-based and Sb-based. Halide substitution in $Cs_3Bi_2(Cl_{1-x}I_x)_9$ VOPs generates a coherent structural and electronic response that is consistently observed across the studies of Mehmood et al., McCall et al., and Morgan et al.[7−9] Both the Cl-substitution in $Cs_3Bi_2I_9$, explored by McCall and Mehmood, which yields the ordered bilayer phase $Cs_3Bi_2I_6Cl_3$, as well as the I-substitution in $Cs_3Bi_2(Cl_{1-x}I_x)_9$, examined by Morgan, lead to the same layered $P\bar{3}m1$ topology. In this structure, I^- preferentially occupies capping sites, while Cl^- stabilizes bridging positions (as per Figure 2a,b), converting the structure from isolated $[Bi_2I_9]^{3-}$ dimers to corner-connected bilayers, resulting in the conversion of 0D $Cs_3Bi_2I_9$ to 2D $Cs_3Bi_2I_6Cl_3$. This configuration has been experimentally verified via synchrotron X-ray diffraction (XRD) and Raman spectroscopy, where the vibrational fingerprints shift from 0D dimer or 1D chain modes to those characteristics of an extended octahedral lattice. In $Cs_3Bi_2I_6Cl_3$, the terminal Bi−I (2.9034 Å) and bridging Bi−Cl (2.9262 Å) bond lengths are nearly identical, as shown in Figure 2c. This equalization shifts the Bi atom significantly closer to the center of the octahedron, creating a more symmetric environment than in the parent compound ($Cs_3Bi_2I_9$).

Diffuse-reflectance UV−vis shows an absorption edge at 2.07 eV (Tauc plot analysis), essentially unchanged from $Cs_3Bi_2I_9$, which is 2.06 eV, but DFT (VASP, PBEsol + SOC) reveals the band gap becomes direct (1.38 eV) in $Cs_3Bi_2I_6Cl_3$ with this dimensional expansion, as shown in Figure 2d. As stated in Table 1, the calculated gap of 1.38 eV is underestimated relative to the absorption edge of 2.07 eV, but their difference is quite similar to that of the isostructural $Cs_3Sb_2I_9$ using the same functional (1.2 vs 1.89 eV absorption edge), validating the DFT results. Furthermore, the DOS analysis reported by both Morgan and McCall (Figure 2e) revealed that the valence band is primarily dominated by I-p, while the conduction band is mainly contributed by Bi 6p states, with minimal Cl states at the edges. This emphasizes why the absorption edge does not exhibit a significant blue

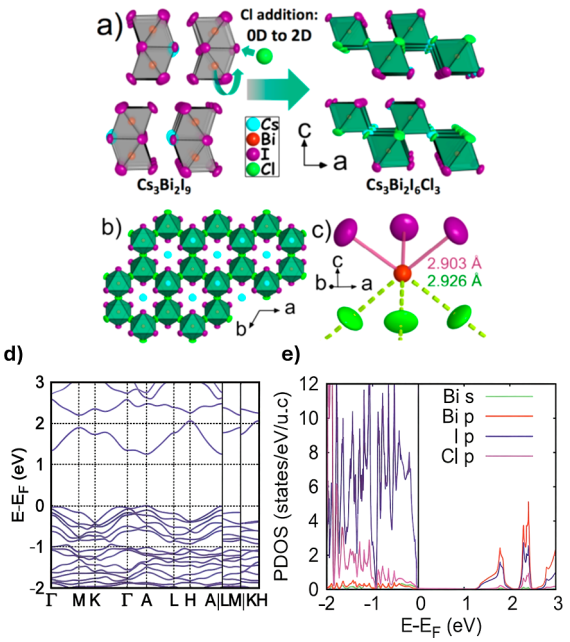

Figure 2. $Cs_3Bi_2I_6Cl_3$ structure: (a) structure comparison of 0D $Cs_3Bi_2I_9$ and 2D $Cs_3Bi_2I_6Cl_3$ viewed down the *b*-axis. The latter is a bilayered defect perovskite structure. (b) $Cs_3Bi_2I_6Cl_3$ viewed along the *c*-axis. (c) Coordination environment of Bi^{3+} in the $[BiCl_6/2I_3]^{3-}$octahedron. (d) Electronic band structure and (e) projected density of states (DOS). Reproduced with permission from ref 8. Copyright 2019 American Chemical Society.

shift despite the incorporation of Cl at the bridging sites: the optical transition remains governed by I−Bi antibonding interactions at the terminal sites, rather than by the Bi−Cl−Bi bridges. In other words, charge transport is still largely controlled by the iodide-derived antibonding network, while Cl mainly modifies the interlayer connectivity and the transport anisotropy, as shown in Figure 2b. This anisotropic role of Cl is also reflected in the calculated effective masses. Replacing Cl by I in the same structural framework reduces the calculated out-of-plane effective masses from 0.63 m_0 to 0.39 m_0 for electrons and from 1.8 m_0 to 0.41 m_0 for holes, showing that halide ordering quantitatively influences the band dispersion and the carrier mobility-related descriptors. Further, these results show that Cl enhances transport anisotropy and restricts the interlayer carrier motion, whereas iodide promotes stronger interlayer orbital overlaps. However, although the 2D structure provides greater 2D structural connectivity, the material still exhibits strong self-trapped exciton (STE) recombination and very strong electron−phonon coupling, quantified by a Huang−Rhys factor of 212 ± 12 and an LO-phonon coupling constant of 291.8 ± 61.9 meV.[8] These values indicate strong carrier localization and favor broad phonon-assisted and nonradiative recombination pathways, which limit the full transport advantage expected from higher structural dimensionality.

In $Cs_3Bi_2(Cl_{1-x}I_x)_9$, XRD revealed that even a minor substitution of iodine into the chloride lattice initiates a transformation from the 1D chain-like structure of $Cs_3Bi_2Cl_9$ to a 2D layered perovskite topology.[9] This transition arises from the larger ionic radius and higher polarizability of I^-, which alter the Bi−X bonding network and favor extended octahedral connectivity. UV−vis spectroscopy confirmed a strong redshift of the absorption edge as iodine content increased, with the

https://doi.org/10.1021/acsomega.6c01559
ACS Omega 2026, 11, 30219−30235

Table 1. Different Mixed-Halide VOP-Based Optoelectronic Devices, Synthesis Methods, Bandgap, Performance, and Stability Matrices

material	thin film synthesis method	structure	bandgap (eV)	extraction method	photophysics metrics	device architecture	performance	stability condition	reference
$Cs_3Bi_2I_6Cl_3$		2D ($P\bar{3}m1$)	1.38 (direct)	DFT (PBESol + SOC)	-	-	-	-	8
	sealed-tube melt synthesis	2D ($P\bar{3}m1$)	2.07 (direct)	Tauc method	PL peak- 25 mW				
		2D ($P\bar{3}m1$)	2.07 (direct)	DFT (GGA+ (TB-mBJ)	-	FTO/PBCM-SnS_2/ $Cs_3Bi_2I_6Cl_3$/NiO/Ni (solar cell)	31.27% (SCAPS simulated)	-	7
	solution-acid synthesis	2D ($P\bar{3}m1$)	1.87 (direct)	DFT (PBE + SOC)	-	-	-	-	9
$Cs_3Bi_2I_6Br_3$	solution-based spin-coating technique	2D layered	2.05 (direct)	Tauc method	-	ITO/NiO_x/ $Cs_3Bi_2I_6Br_3$/ PCBM/C_{60}/BCP/Ag (solar cell)	1.15% (experimental)	82% initial PCE, 400 h, 50% RH, 26 °C, AM 1.5 G solar illumination (unencapsulated)	16
$Cs_3Bi_2I_6Br_3$	solution-based spin-coating technique	2D ($P\bar{3}m1$)	2.07	Tauc method	-	ITO/PEDOT/PSS/ $Cs_3Bi_2I_6Br_3$/C60/BCP/Ag (photodetector)	photosensitivity of 4.1×10^4 at zero bias, as well as the responsivity and detectivity arriving to 15 mA/W and 4.6×10^{11} Jones	96% initial photocurrent, 100 h 25−40% RH, 25 °C (Unencapsulated)	19
$Cs_3Bi_2I_6Br_3$	two-step solvent evaporation method	2D ($P\bar{3}m1$)	-	-	-	Cr/$Cs_3Bi_2I_6Br_3$/Pt (passivated with BiOBr nanosheets) (X-ray detector)	sensitivity: 0.4 μCGy_{air} cm^2	-	27
$Cs_3Sb_2Cl_6Br_3$	solution-acid synthesis	2D ($P\bar{3}m1$)	2.07 (direct)	DFT (PBE)	-	-	-	-	5
$Cs_3Sb_2Cl_3Br_6$	solution-acid synthesis	2D ($P\bar{3}m1$)	2.03 (direct)	DFT (PBE)	-	-	-	-	
$Cs_3Sb_2Cl_6I_3$	solution-based spin coating	2D layered ($P\bar{3}m1$)	2.05 (direct)	Tauc method	hall mobility- 5.7 $cm^2 V^{-1} s^{-1}$	FTO/c-TiO_2/m-TiO_2/ $Cs_3Sb_2Cl_3I_6$/poly-TPD/Au	PCE- 1.56% (experimental)	90% initial PCE, 33 days, AM 1.5 G solar illumination (placed in N_2 -filled glovebox)	13
						FTO/c-TiO_2/m-TiO_2/ $Cs_3Sb_2Cl_3I_6$/ LZ-HTL-1−1/ Au (solar cell)	PCE- 2.15% EQE - 62.5% (experimental)	-	
$Cs_3Sb_2ClxI_{9-x}$	solution-based spin coating	2D ($P\bar{3}m1$))	1.95 (quasi-direct)	Tauc method		FTO/c-TiO_2/m-TiO_2/ $Cs_3Sb_2Cl_3I_6$/poly-TPD/Au (indoor photovoltaics)	PCE (Indoor −1000 lx): fluorescent light (FL)- 4.9% (experimental)	-	20
$Cs_3Sb_2Cl_6I_3$	modified solution-based spin-coating technique	2D ($P\bar{3}m1$)) (direct)	1.95 (direct)	Tauc method	carrier lifetime −11.14 ns	PET-ITO/$Cs_3Sb_2Cl_3I_6$/ PDMS/Ni (perovskite-based triboelectric nanogenerator)	power density 2.13 Wm^{-2} under AM 1.5 G illumination (experimental)	90.9%, initial triboelectric output, 40 days, 40 °C	25
$Cs_3Sb_2Br_{3.5}I_{6.5}$	mechanochemical solid-state synthesis	2D ($P\bar{3}m1$	1.98 (direct)	Tauc method	-	-	-	-	14
$Rb_3Bi_2I_6Cl_3$	-	2D ($P\bar{3}m1$	2.051 (direct)	DFT		FTO/TiO_2−SnO_2/ $Rb_3Bi_2I_6Cl_3$/MoO_3/Ni (solar cell)	11.39% (SCAPS simulated)	-	10
$Rb_3Bi_2I_3Cl_6$	-	2D 2D ($P\bar{3}m1$	1.996 (Indirect)	DFT	-	FTO/TiO_2−SnO_2 /$Rb_3Bi_2I_3Cl_6$/MoO_3/Ni (solar cell)	11.52% (SCAP simulated)	-	10
	sealed-tube melt synthesis		2.02 (direct)	Tauc method	-	-	-	-	8
$Rb_3Sb_2Br_9$ $Rb_3Sb_2Br_{9-x}I_x$	solution-based antisolvent vapor diffusion crystallization method	2D layered P 21/n	2.46	Tauc method	-	glass/ITO/c-TiO2/mp-TiO_2/ $Rb_3Sb_2Br_{9-x}I_x$/spiro-OMeTAD/Au. (solar cell)	1.37% (x = 9) (experimental)	84% of initial PCE, 150 days, 100 mW/cm2. (stored in the glovebox in the dark)	26

https://doi.org/10.1021/acsomega.6c01559
ACS Omega 2026, 11, 30219−30235

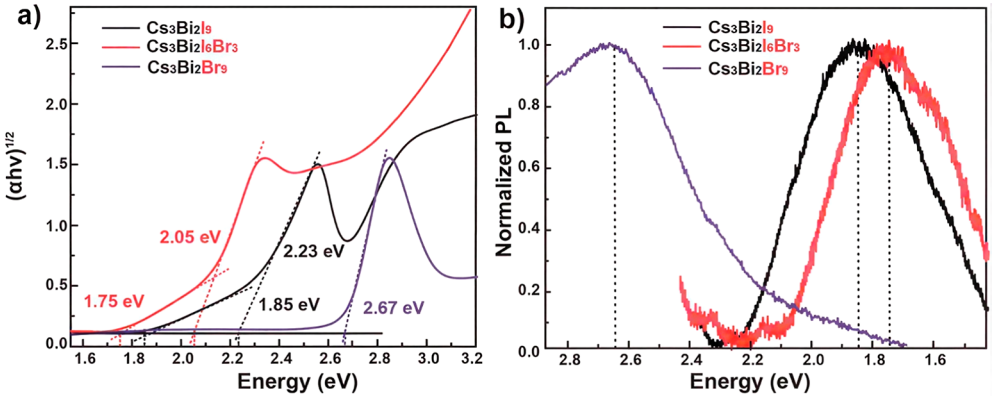

Figure 3. (a) Tauc plots of absorbance and (b) PL measurement of $Cs_3Bi_2I_9$, $Cs_3Bi_2I_6Br_3$, and $Cs_3Bi_2Br_9$ films. Reproduced from ref 16 with permission from the Royal Society of Chemistry.

optical bandgap narrowing from 2.8 eV (Cl-rich) to 1.7 eV (I-rich), reflecting enhanced visible-light absorption. DFT calculations had been conducted to reproduce this bandgap reduction. The results revealed that the reduction can be attributed to the downshift of halide-derived p-orbitals and increased Bi−I orbital overlap, which enhances the band dispersion and the carrier delocalization. Bonding asymmetry due to the stereochemically active lone pair on the Bi atom is likely one reason for the preference for iodine occupation on the capping sites.

Morgan et al. observed the same ordering tendency in $Cs_3Bi_2Cl_{8\cdot16}I_{0\cdot84}$, where the compound adopts the 2D trigonal $P\bar{3}m1$ vacancy-ordered structure with a unit cell volume 3.8% smaller than β-$Cs_3Bi_2Cl_9$. Importantly, even limited I incorporation in $Cs_3Bi_2(Cl_{1-x}I_x)_9$ (x = 0.09−0.52) is sufficient to switch the crystal from the 1D *Pnma* framework to the 2D $P\bar{3}m1$ phase, accompanied by an immediate 0.5 eV decrease in the absorption edge, followed by a nearly linear redshift with further I incorporation. However, calculations show that dimensionality alone cannot account for this change because the PBE band gap decreases only from 2.32 eV for 1D $Cs_3Bi_2Cl_9$ to 2.09 eV for hypothetical 2D $Cs_3Bi_2Cl_9$, whereas HSE predicts a broader 2.8 to 1.7 eV evolution across the Cl-rich to I-rich compositions. The dominant effect arises from site-selective bonding: Bi−I interactions are much stronger at the 6i capping site than at the 3e site, with integrated crystal orbital Hamilton population values of −3.4 eV and −2.1 eV, respectively, compared with −2.5 eV and −1.5 eV for Bi−Cl. This also explains why $Cs_3Bi_2Cl_6I_3$ has a lower band gap than $Cs_3Bi_2Cl_3I_6$ despite containing less iodine overall: halides at both 6i and 3e sites raise the valence band maximum (VBM) through Bi-s/halide-p antibonding, but only the 6i site contributes significantly to Bi-p/halide-p antibonding at the conduction band minimum (CBM), making iodine on the capping site electronically more effective in narrowing the gap.[9] Thus, prior studies consistently indicate that preferential iodine occupation at capping sites, chlorine retention at bridging sites, and halide-driven 1D-to-2D connectivity together enhance the orbital coupling, band dispersion, and bandgap narrowing, with likely implications for improved carrier transport and modified recombination pathways.

When device performance is considered, these structural and electronic changes also translate to more favorable simulated photovoltaic metrics. Theoretical device modeling by Mehmood et al. predicted that a properly engineered $Cs_3Bi_2I_6Cl_3$ absorber could surpass the performance of its 0D $Cs_3Bi_2I_9$ counterpart, with simulated device efficiency surpassing 30%.[7] SCAPS-1D modeling of an FTO/PCBM-SnS_2/$Cs_3Bi_2I_6Cl_3$/NiO/Ni heterostructure yields impressive, simulated device parameters: short circuit current (J_{sc}) of 23.35 mA cm^{-2}, open circuit voltage (V_{oc}) of 1.47 V, fill factor (FF) of 90.97%, and PCE of 31.27%.[7] For comparison, a $Cs_3Bi_2I_9$-based solar cell (glass/FTO/ETL/$Cs_3Bi_2I_9$/HTL/Au) recorded an efficiency of 13.81%,[1] underscoring the substantial performance advantage gained through Cl-induced dimensional and electronic restructuring.

However, PCE values based on numerical modeling are significantly higher than the experimentally demonstrated efficiency. The simulations were conducted assuming optimized device parameters, including low defect densities, ideal interface properties, and favorable band alignment between the absorber and transport layers. In contrast, the experimentally reported efficiency values remain below 2−3% [for $Cs_3Bi_2I_9$, experimentally reported PCE 0.71% and 1.09%], primarily due to the high defect densities, the limited carrier mobility, and the nonideal interface energetics that promote recombination losses.[15]

The overall results show the site-selective halide ordering and the halide-driven dimensionality control influence on the band gap character, band-edge orbital composition, effective mass, transport anisotropy, and recombination strength of mixed-halide VOPs. The transition from isolated dimers/chains to layered frameworks can promote more favorable band topology, including indirect to direct gap conversion and improved orbital connectivity. However, the persistence of strong electron−phonon coupling and self-trapped excitons (STEs) means that gains in structural dimensionality do not translate directly into proportionate improvements in carrier mobility or suppressed recombination. Thus, the optoelectronic response of mixed-halide VOPs is governed by a balance between enhanced structural connectivity and the carrier localization arising from lattice couplings and defects.

3.1.2. Bi-Based I/Br Mixed-Halide Systems. Yu et al. and Bonomi et al. proved that systematic alloying of Br into $Cs_3Bi_2I_9$ can effectively tune the optoelectronic properties and alter the crystallographic phase stability.[6,16] When the $Cs_3Bi_2I_9$ compound is alloyed with Br, the structure undergoes a phase transition from $P6_3/mmc$ (0D) (I-rich) to $\bar{P}3m1$ (2D layered, Br-rich), leading to a narrower 2.03 eV direct band gap versus 2.20 eV for $Cs_3Bi_2I_9$. This experimental band gap is calculated from the Tauc plot analysis. The equation $(kh\nu)^{1/n} = C(h\nu - E_g)$ is used for the analysis of the band gap, where k is the

https://doi.org/10.1021/acsomega.6c01559
ACS Omega 2026, 11, 30219−30235

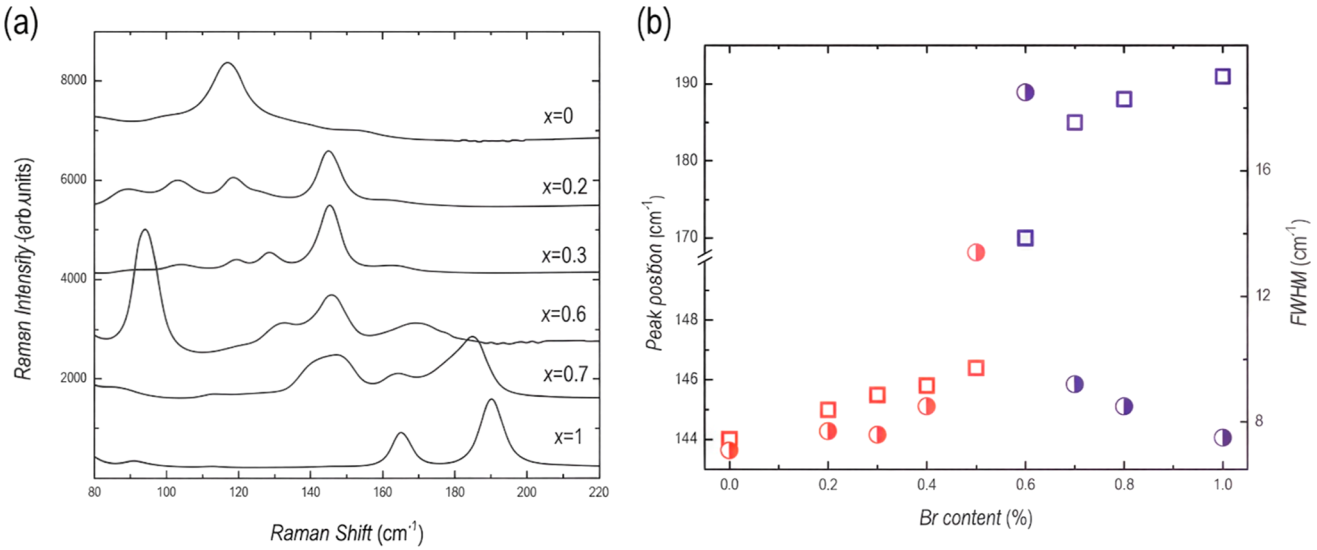

Figure 4. (a) Raman spectra at room temperature of different mixed samples plotted with the two endmembers and (b) peak position (open symbols) and fwhm (full symbols) for the Raman bands corresponding to A′ mode in $Cs_3Bi_2I_9$ (squares) and to A_1g mode in $Cs_3Bi_2Br_9$ (circles). Reproduced with permission from ref 6. Copyright 2021, American Chemical Society.

absorption coefficient, h is Planck's constant, C is the proportionality constant, ν is the frequency of light, E_g is the band gap, and n is 1/2 and 2, expressing the indirect or direct band gap of the substance, respectively. The tau plots of $(kh\nu)^2$ vs $h\nu$ and the plot of $(kh\nu)^{1/2}$ vs $h\nu$ were used for the calculation of the direct band gap and indirect band gap of the given compounds, respectively. In $Cs_3Bi_2I_9{-}_xBr_x$ ($0 \leq x \leq 9$), $Cs_3Bi_2I_6Br_3$ seems to be the phase transition tipping point from $P6_3/mmc$ to $\bar{P}3m1$ when the Br content increases.[7] In $Cs_3Bi_2I_{1-x}Br_x$, the crystal structure transformation typically occurs around x = 0.4−0.5, accompanied by a systematic contraction of lattice parameters due to the smaller ionic radius of Br compared to I.[6] The lattice evolution and boundary are clearly observed by XRD, as peak positions shift to higher angles and new reflections emerge, confirming the initiation of reorganization in the structure.

UV−vis absorption measurements of $Cs_3Bi_2I_{9-x}Br_x$ films evidence a characteristic evolution in bandgap with Br incorporation. As demonstrated in Figure 3a, a red shift is observed up to x = 3, where the bandgap decreases from 2.23 eV (x = 0) to 2.05 eV ($Cs_3Bi_2I_6Br_3$), reflecting the onset of layered connectivity and enhanced electronic coupling. This indicates that the structural transition increases octahedral connectivity and Bi−X orbital overlap, thereby enhancing the band dispersion and reducing carrier localization.

Beyond this composition, further Br-substitution induces a progressive blue shift, with the bandgap widening to 2.67 eV in $Cs_3Bi_2Br_9$, consistent with stronger Bi−Br bonding and reduced orbital overlap as shown in Figure 3.[7] In $Cs_3Bi_2(I_1{-}_xBr_x)_9$ ($0 \leq x \leq 1$), the direct bandgap increases nearly linearly with Br content, showing only a slight deviation near x = 0.5, where Raman spectroscopy confirms the presence of mixed I^- and Br-centered octahedra.[6] The steady state PL emission spectrum shown in Figure 3b also validates the bandgap values determined in Figure 3a. Here, it is necessary to note that a 480 nm laser near their optical band gaps was used to excite the $Cs_3Bi_2I_9$ and $Cs_3Bi_2I_6Br_3$ films due to the excitation−emission coupling effect in the Bi-based perovskite materials. For $Cs_3Bi_2I_9$, the excitation wavelength was changed to 405 nm, and its emission peak appears at 2.64 eV, which is aligned with the bandgap (2.67 eV) determined in Figure 3a. For $Cs_3Bi_2I_9$ and $Cs_3Bi_2I_6Br_3$ films, their major emission peaks are indexed at 1.84 and 1.74 eV, which match well with the indirect bandgap values shown in Figure 3a. The broad shape of PL emission peaks can be ascribed to the phonon scattering along with surface recombinations.

This combined red-to-blue optical trend matches previously reported behavior by McCall et al.,[8] establishing halide alloying as a powerful and precise means of tuning absorption edges and electronic structure in lead-free bismuth halide perovskite analogues.

Ultraviolet photoelectron spectroscopy (UPS) of $Cs_3Bi_2I_{9-x}Br_x$ provided data on the energy level alignment. VBM increased with increasing Br content, as would be expected for the increased electronegativity of Br^- and consistent with the blue shift observed in high x value optical absorption. VASP calculations, which were conducted according to PBE + SOC, reproduced experimentally measured bandgap behavior as stated in Table 1. The valence band was populated with the p states of the halides (I/Br), while the conduction band was derived mainly from Bi6p orbitals. Increasing Br content reduces orbital overlap but enhances lattice stability. Crucially, the $P6_3/mmc$ to $\bar{P}3m1$ phase transition was identified as the key driver of the bandgap reduction near x = 3 due to enhanced 2D connectivity and band dispersion.[7] Thus, halide alloying influences the band structure not only through composition but also through changes in phase symmetry, octahedral connectivity, and local bonding environment. Because the band dispersion is directly related to carrier effective mass, this structural reorganization is also expected to influence the carrier mobility and transport pathways.

Raman spectroscopy, in $Cs_3Bi_2(I_{1-x}Br_x)_9$, increasing substitution of bromine for iodine causes differential vibrational and structural modifications that delineate the phase transition from $Cs_3Bi_2I_9$ to $Cs_3Bi_2Br_9$ phase, as shown in Figure 4a,b. Raman spectra at low Br composition remain characterized by the Bi−I symmetric vibration (A′ mode), indicating retention of the I-rich lattice but with an altered orientation. With rising Br concentration, more Bi−Br vibrational modes emerge above

https://doi.org/10.1021/acsomega.6c01559
ACS Omega 2026, 11, 30219−30235

160 cm^{-1} with a smooth blue composition shift. Both Bi−I and Bi−Br bands are visible in the intermediate range ($0.3 < x < 0.6$), showing the mixed-phase regime with disordering. At higher concentrations of Br, the Bi−I contribution vanishes, while sharper Bi−Br structures dominate, reflecting the formation of the trigonal $Cs_3Bi_2Br_9$-type phase. In general, Raman evolution confirms that Br incorporation causes lattice contraction, phonon hardening, and increasing crystallographic order, which is an I-rich to Br-rich structure transition.[6] At the same time, the mixed-composition regime implies local structural disorder and mixed octahedral environments, which can introduce carrier scattering and nonradiative recombination channels even when the average crystal symmetry becomes more favorable.

$Cs_3Bi_2I_6Br_3$ thin films demonstrate a pure phase with optimal crystalline quality in the scanning electron microscopy (SEM) micrographs and the minimum bandgap (2.02 eV), emphasizing its best qualities for photovoltaics. Visual evolution of films followed these electronic changes, from deep red for I-rich to orange-yellow for intermediate Br composition to bright yellow for Br-rich films. SEM imaging of $Cs_3Bi_2I_{9-x}Br_x$ ($0 \le x \le 9$) showed a transition from porous, vertical flake-like grains for iodide-rich films to tightly packed grains for $x = 3$ ($Cs_3Bi_2I_6Br_3$), reflecting the improved film quality, resulting in reduced trap-assisted losses and more efficient charge extraction. In addition to that, when decreasing the I/Br ratio, the film appearance of grains gets clearer, and the grain size becomes larger when the ratio is 0/9.[7] Besides the phase transition, which may be attributed to the high concentration of Br ions, which also play a crucial role in enhancing film quality in halide perovskite films.[6] Furthermore, the addition of chlorobenzene as an antisolvent in the spin coating process improved surface compactness and smoothness, resulting in reduced trap states and improved device performance.[17,18]

Complementary, atomic force microscopy analysis of $Cs_3Bi_2(I_{1-x}Br_x)_9$ ($0 \le x \le 1$) films follows the same trends. Grain size increases with Br inclusion, 40−70 nm in $Cs_3Bi_2I_9$ to 200−300 nm in $Cs_3Bi_2Br_9$, suggesting enhanced lateral crystal growth and greater grain fusion in Br-rich films.[6] Although Br-rich films are less compact, this might be consistent with the trigonal layered structure; surface morphology is relatively homogeneous across the composition range. These results indicate that bromine substitution is primarily impacting the grain growth and the packing density, but maintaining smooth, intact film morphology, highlighting the structural robustness and scalability of Br and I mixed thin films for lead-free optoelectronic applications. From a device perspective, such microstructural changes are important because larger grains and improved phase purity reduce grain-boundary-assisted recombination and facilitate carrier transport across the film.

These film quality improvements are reflected experimentally in a planar device. Yu et al. experimentally fabricated planar heterojunction devices with the configuration ITO/NiO_x/absorber/PCBM/C_{60}/BCP/Ag, which demonstrated a precise composition−performance relationship. The optimized $Cs_3Bi_2I_6Br_3$ ($x = 3$) composition achieved the highest PCE of 1.15%, with J_{sc} of 3.15 mA cm^{-2}, V_{oc} of 0.64 V, and FF of 0.57. In contrast, pure $Cs_3Bi_2I_9$-based PSC delivered only 0.23% experimental PCE. In the device operational stability investigations, the unencapsulated $Cs_3Bi_2I_6Br_3$-based device was able to maintain 82% of the original PCE after continuous soaking under AM 1.5 G solar illumination at approximately 26 °C and 50% relative humidity, compared with the remaining 75% of the control $Cs_3Bi_2I_9$-based device.[7]

In another study, similar results were reported by Liu et al., in which $Cs_3Bi_2I_{9-x}Br_x$ was investigated for photodetector application. As Br content increases, the material evolves from the $P6_3/mmc$ phase of $Cs_3Bi_2I_9$ to the $P\text{-}3m$ phase of $Cs_3Bi_2I_6Br_3$, with a clear transition at $x = 3$, which can be attributed to three Br ions occupying the bridging positions to form a stable mixed structure as previously discussed in $Cs_3Bi_2I_6Cl_3$. The structural reorganization upon Cl-substitution is accompanied by a pronounced optical change: $Cs_3Bi_2I_6Br_3$ exhibits the reddest absorption edge at 590 nm, whereas further Br-rich compositions shift back to 465 nm, and the optimized $Cs_3Bi_2I_6Br_3$ film shows a band gap of 2.07 eV compared with 2.68 eV for $Cs_3Bi_2Br_9$. Importantly, the phase transition also transforms the film from poorly connected plate-like morphologies to a dense, flat, highly crystalline film, which is directly linked to superior carrier collection and self-powered photodetector performance. The $Cs_3Bi_2I_6Br_3$ device delivers 4.1×10^4 photosensitivity, 15 mA W^{-1} responsivity, 4.6×10^{11} Jones detectivity, 4.5 μA short-circuit current, 0.61 V open-circuit voltage, and fast rise/decay times of 40.7/27.1 ms at zero bias. To evaluate device operational stability, the unencapsulated $Cs_3Bi_2I_6Br_3$-based photodetector was aged in ambient conditions at 25−40% RH and approximately 25 °C. After 100 days, the photocurrent decreased only from 4.56 to 4.40 mA, retaining over 96% of its initial value.[19]

Overall, in $Cs_3Bi_2I_{9-x}Br_x$, there is a clear phase-transition tipping point where the structure changes from 0D to a 2D layered phase; up to this point, increasing Br content narrows the bandgap (red shift) and strengthens visible-light absorption as connectivity and band dispersion improve, whereas beyond it, further Br incorporation into the Br-rich layered phase leads to bandgap widening (blue shift) and absorption shifting to higher energies, together with a more contracted and ordered lattice. Thus, site-selective halide substitution and halide-driven dimensionality control quantitatively influence not only the bandgap magnitude but also the phase symmetry, the orbital overlap, the carrier delocalization, the transport pathways, and recombination losses in mixed-halide VOPs.

3.1.3. Sb-Based I/Br Mixed-Halide Systems. The Cs- and Sb-based mixed-halide perovskite materials are also attracting attention as potential Pb alternative materials in different optoelectronic applications. Giovilli et al. demonstrated that the mixed-halide $Cs_3Sb_2(Br_{1-x}I_x)_9$ solid solution provides an effective pathway for tuning the bandgap of lead-free antimony perovskites through the controlled halide substitution.[14] As bromine is progressively replaced by iodine, a monotonic redshift of the absorption edge and a reduction of the optical bandgap are observed, from 2.50 eV ($x = 0$) for $Cs_3Sb_2Br_9$ to 1.95 eV ($x = 1$) for $Cs_3Sb_2I_9$. Values of the direct and indirect band gaps were determined from the Tauc plots.

Intermediate compositions show a pronounced bowing behavior, with the largest bandgap drop (0.3−0.4 eV) occurring around $x = 0.5$, where both halides coexist in comparable fractions. The bandgap contraction arises from the larger ionic radius and lower electronegativity of I^- relative to Br^-, which expands the lattice and enhances the overlap between Sb 5s/5p and I 5p orbitals, thus raising the valence-band maximum (VBM) while keeping the conduction band mostly Sb 5p-derived. Consequently, the electronic transition of energy declines when decreasing the Br/I ratio.

https://doi.org/10.1021/acsomega.6c01559
ACS Omega 2026, 11, 30219−30235

This compositional dependence is experimentally verified through different characterization techniques. XRD patterns show a systematic shift of peaks to the lower 2θ angles with increasing iodine content, confirming the unit-cell expansion and the solid-solution formation in agreement with Vegard's law. Quantification of this lattice expansion (cell volume expanding from 525 Å^3 to 637 Å^3) is given by Rietveld refinement of the XRD data, which also confirms the single-phase $\bar{P}3m1$ layered structure for all compositions. A progressive redshift of Sb−X vibrational modes is shown by Raman spectroscopy modes; specifically, the A_1g mode at 210 cm^{-1} in $Cs_3Sb_2Br_9$ softens to 185 cm^{-1} for intermediate members, then disappears as I-dominated vibrations emerge at 149−166 cm^{-1} in $Cs_3Sb_2I_9$, pointing to lattice softening and heavier halide substitution. UV−vis diffuse reflectance spectroscopy and Tauc plot analysis confirm the continuous redshift in the absorption edge and bandgap narrowing (direct E_g from 2.50 to 1.95 eV; indirect E_g from 2.31 to 1.67 eV). These optical and structural results are self-consistent, proving that halide substitution successfully modulates the electronic structure of the material without compromising crystallographic integrity.[14]

From a mechanistic standpoint, the bandgap reduction can be attributed to (i) the lower bonding energy of Sb−I vs Sb−Br, (ii) enhanced orbital hybridization between Sb 5s and I 5p states, and (iii) lattice expansion, which modulates the crystal-field splitting. Together, these factors narrow the electronic gap and extend visible-light absorption toward 650 nm.[14] Thus, the $Cs_3Sb_2(Br_{1-x}I_x)_9$ system enables smooth, composition-controlled tuning of optoelectronic properties, verified through consistent XRD, Raman, and UV−vis evidence, making it a promising platform for photodetectors, photocatalysts, and lead-free solar absorbers.

3.1.4. Sb-Based Cl/Br Mixed-Halide Systems. Building on related chemistry, Pradhan et al. synthesized $Cs_3Sb_2Cl_{9-x}Br_x$ solid solution through a controlled solution-based ion-exchange route where the gradual addition of HBr into HCl allows in situ substitution of Cl^- by Br^- as confirmed by PXRD (Powder XRD), SEM, energy dispersive X-ray spectroscopy (EDX), and Raman analyses.[5] Pradhan et al. have discussed an indirect to direct band gap transition in $Cs_3Sb_2Cl_{9-x}Br_x$ with Br-substitution and provided possible explanations based on the experimental and theoretical studies. Substitution of Br in $Cs_3Sb_2Cl_{9-x}Br_x$ affects the band gap depending on its position in the structure. The band gap obtained via DFT calculations for the $Cs_3Sb_2Cl_9$ and $Cs_3Sb_2Br_9$ is 2.28 and 1.83 eV, respectively. Furthermore, $Cs_3Sb_2Cl_9$ is determined as an indirect band gap compound based on DFT band structure. Substitution of two Br^- ions in $Cs_3Sb_2Cl_{9-x}Br_x$ results in the transition from an indirect to a direct band gap. It may be noted that there are two crystallographic positions of the chloride ion, bridging (three) and terminal positions(six), in $Cs_3Sb_2Cl_9$. Substituting Br completely (all the three) at the bridging position does not alter the band type and retains the indirect band gap; however, partial substitution at the terminal position results in a transition from the indirect to direct band gap in $Cs_3Sb_2Cl_{9-x}Br_x$ with $x = 2$. From the Rietveld refinement, it is also observed that initially, Br prefers to replace the terminal chlorine atoms, and a higher percentage of Br-substitution leads to the replacement of bridging chlorine atoms in $Cs_3Sb_2Cl_{9-x}Br_x$. The band structure calculations show that the indirect band is retained until $Cs_3Sb_2Cl_8Br$ as the conduction band minima and valence band maxima lie at two different k-points. However, $Cs_3Sb_2Cl_7Br_2$ shows a direct band gap as both the CBM and the VBM lie at the same k-point. The band gap of higher Br-substituted compounds remains direct ($Cs_3Sb_2Cl_3Br_6$ = 2.03 eV and $Cs_3Sb_2Cl_6Br_3$ = 2.07 eV).

Rietveld refinement of the PXRD data provides important insight into the site preference of Br. At low substitution levels, Br^- ions preferentially occupy terminal sites in SbX_6 octahedra and later occupy bridging sites. This site-selective substitution of Br induces lattice expansion and structural distortion due to a significant alteration in the terminal Cl/Br−Sb−Cl/Br bond angle. Specifically, the terminal bond angle drops sharply from 94° in $Cs_3Sb_2Cl_9$ to 91° in $Cs_3Sb_2Cl_{8.02}Br_{0.98}$, then gradually increases with further Br incorporation, following a trend similar to the lattice parameter variation. In contrast, the bridging X−Sb−X bond angles show only minor changes and remain nearly constant. Raman results support this site-selective substitution, as shown by new vibrational bands and shifts in the Sb−X stretching modes. Overall, Br-induced distortion of the terminal bond angles is likely an important factor influencing the band gap evolution in $Cs_3Sb_2Cl_{9-x}Br_x$.

To understand the preferential occupancy of Br at the terminal site rather than the bridging site, total energy calculations were performed for a representative composition, $Cs_3Sb_2Cl_6Br_3$. Two configurations were considered: (a) all three Br atoms substituted at the terminal (6i) positions and (b) all three Br atoms substituted at the bridging (3e) positions. The calculations show that Br-substitution at the terminal (6i) positions lowers the total energy by 268 meV relative to that of substitution at the bridging positions. This result supports the experimental observation that Br preferentially occupies the terminal sites over the bridging sites.

DFT calculations also clarify the microscopic origin of the indirect to direct band gap transition. Br-substitution leaves the VBM nearly unchanged, while the CBM shifts from the A-point to the Γ-point, indicating that the band gap-type transition is controlled mainly by changes in the conduction band. Analysis of the projected DOS shows that the conduction band is composed of Sb p, terminal-halide p, and bridging-halide s states, and that partial Br-substitution at the terminal site induces a splitting of the Sb/halide p states above the Fermi level. However, no such phenomena are observed with Br-substitution at the bridging position. By contrast, substitution at the bridging site alone does not induce this splitting and does not change the band gap type. These results show that site-selective halide ordering influences band structure through the bond-angle distortion, the conduction-band splitting, and the k-space relocation of the CBM, which is expected to affect carrier transport by altering the band dispersion and modifying the recombination pathways by changing whether the lowest transition is indirect or direct. In addition to tuning the band structure, Br-substitution also improves the intrinsic material stability of $Cs_3Sb_2Cl_{9-x}Br_x$. In addition to that, Pradhan et al. showed by TGA that the thermal stability gradually increases with increasing Br incorporation, while representative mixed-halide compositions such as $Cs_3Sb_2Cl_6Br_3$ and $Cs_3Sb_2Cl_3Br_6$ remained stable even after 15 days of sunlight exposure.[5] The retention of phase integrity in PXRD after prolonged illumination further confirms that halide mixing enhances the robustness of these mixed-anion antimony perovskites.

In all, Br-substitution serves as an effective way to tune structural dimensionality, intrinsic stability of the materials and

https://doi.org/10.1021/acsomega.6c01559
ACS Omega 2026, 11, 30219−30235

device operational stability, and optoelectronic response and thus points toward halide mixing as a practical route to optimize lead-free perovskite absorbers.[5]

3.1.5. Sb-Based I/Cl Mixed-Halide Systems. Several studies have demonstrated that substituting Cl into $Cs_3Sb_2I_9$ markedly modifies its optoelectronic properties, enabling controlled tuning of bandgap, structure, and carrier dynamics. These tunable features make Cl-alloyed $Cs_3Sb_2I_9$ highly adaptable for a wide range of optoelectronic applications.[13,20] Peng et al. introduced a low-temperature, solution-based halide exchange method to transform zero-dimensional $Cs_3Sb_2I_9$ into two-dimensional mixed-halide perovskites $Cs_3Sb_2Cl_xI_{9-x}$ ($x \leq 4$). The partial substitution of iodine with chlorine induced a pronounced structural transition from the dimeric 0D phase to a layered 2D vacancy-ordered framework, with optimal compositions at $Cs_3Sb_2Cl_2I_7$ and $Cs_3Sb_2Cl_3I_6$.[13] XRD revealed the gradual disappearance of the 27.7° dimer-phase peak and the emergence of characteristic doublet reflections near 26–30°, confirming the formation of the layered phase as shown in Figure 5a. Optical absorption spectroscopy exhibited both

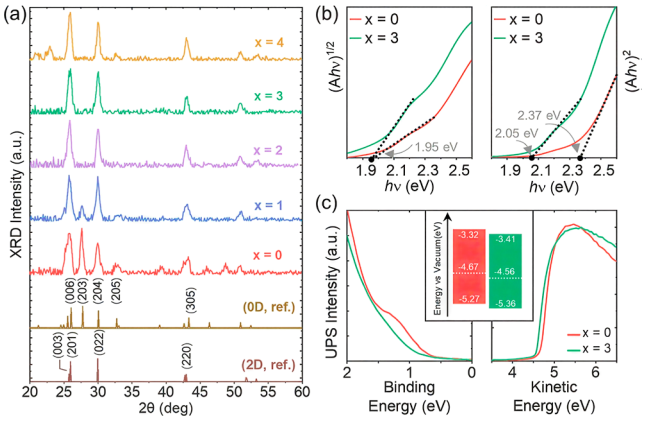

Figure 5. (a) Measured XRD patterns from $Cs_3Sb_2Cl_xI_{9-x}$ thin films (x = 0–4), along with reference patterns for 0D and 2D $Cs_3Sb_2I_9$. (b) Tauc plots of $Cs_3Sb_2I_9$ (0D) and $Cs_3Sb_2Cl_3I_6$ (2D). (c) UPS intensity (valence band states (left) and He I secondary electron cutoff(right)) from $Cs_3Sb_2I_9$ (0D) and $Cs_3Sb_2Cl_3I_6$ (2D) films. Inset: energy levels combining the findings from UPS and UV–vis measurements, assuming negligible excitonic effects. Reproduced with permission from ref 13. Copyright 2020, Elsevier Ltd.

direct and indirect transitions, with the direct band gap (derived from Tau plots) reducing from 2.37 eV ($Cs_3Sb_2I_9$) to 2.05 eV ($Cs_3Sb_2Cl_3I_6$), an energy gap perfectly optimized for top-cell tandem photovoltaics as shown in Figure 5b.

Furthermore, such a bandgap value also aligns with light sources used for indoor photovoltaics[21] and is also suitable for photodetection in the green and blue regions of the visible spectrum.[22] As shown in Figure 5c, UPS measurements indicate work functions of 4.56–4.67 eV and valence-band maxima at around 5.3 eV below the vacuum level, while conduction-band minima were in the range of 3.3–3.4 eV, as for documented layered Sb-halide materials. With their favorable electronic structure, $Cs_3Sb_2Cl_xI_{9-x}$ films exhibited significantly improved photovoltaic and charge transport ability.

When fabricated a sandwich-type device stack (glass/FTO/c-TiO_2/m-TiO_2/$Cs_3Sb_2Cl_3I_6$/poly-TPD/Au), Cl-substitution resulted in 3-fold experimental PCE improvement from 0.24% for $Cs_3Sb_2I_9$ to 1.56% for $Cs_3Sb_2Cl_3I_6$, triggered by improvements of J_{sc} (1.37 to 4.94 mA cm^{-2}), V_{oc} (0.51 to 0.70 V), and FF (34 to 54%). Phase impurities caused by high chlorine ($x \geq 4$) lowered device performance. Optimization of the hole-transport layer by replacing poly-TPD with LZ-HTL-1–1, a higher hole mobility material, again enhanced the PCE to 2.15%, with J_{sc} = 6.46 mA cm^{-2}, V_{oc} = 0.60 V, and FF = 55.7%. This optimization is a 50% enhancement compared to earlier all-inorganic layered Sb-halide perovskites and is almost two times that of the equivalent Bi-based systems.

Importantly, the same structural transformation strongly improves carrier transport, with the hall mobility increasing from 0.5 cm^2 V^{-1} s^{-1} to 5.7 cm^2 V^{-1} s^{-1}. The photocurrent–power analysis showed that both devices are limited by one-center recombination through deep levels, but the much higher mobility of the 2D phase reduces the fraction of carriers lost before collection.[23] Consequently, the peak external quantum efficiency (EQE) increases substantially from 30.7% in the $Cs_3Sb_2I_9$ (0D) device to 62.5% in the $Cs_3Sb_2Cl_3I_6$ (2D) device.

In a follow-up experimental study, the same authors, Peng et al., have utilized $Cs_3Sb_2Cl_xI_{9-x}$ for indoor photovoltaic (IPV) applications.[20] The solution-processed film demonstrated a bandgap value of 1.95 eV, which is close to the optimum value of 1.9 eV for IPV applications. This 2D arrangement of the $Cs_3Sb_2Cl_xI_{9-x}$ promotes efficient in-plane charge transport across covalently linked Sb–I/Cl layers, overcoming limitations typical of other Sb-based PIMs. $Cs_3Sb_2Cl_xI_{9-x}$-based fabricated device exhibits strong spectral overlap with fluorescent and LED indoor light, enabling experimentally obtained PCEs of up to 4.9% under fluorescent (FL) and 4.4% under WLED illumination, compared to about 1.2% under AM 1.5G solar light. These values rival the industry-standard amorphous silicon (a-Si:H),[24] demonstrating its suitability for low-intensity light environments. Remarkably, unencapsulated devices retained and even improved their efficiency after five months of storage in N_2 containing >1000 ppm of O_2 and >500 ppm of H_2O, with PCE increases from 2.3% to 4.9% due to enhanced J_{sc} (50 to 82 μA cm^{-2}) and V_{oc} (0.41 to 0.49 V), implying self-passivation or defect healing over time. Theoretical spectroscopically limited maximum efficiency calculations predict limits of 50–54% for the 2D phase, higher than for a-Si:H, confirming its intrinsic efficiency potential. Together, these results establish $Cs_3Sb_2Cl_xI_{9-x}$ as a stable, eco-friendly, and efficient indoor photovoltaic absorber with strong promise for self-powered IoT sensors, portable electronics, and low-light energy harvesting, positioning it as a leading candidate for next-generation sustainable IPV technologies.

Lead-free antimony halide perovskite $Cs_3Sb_2Cl_3I_6$ possesses great promise for self-powered optoelectronic and triboelectric devices since it is stable with tunable electronic properties. Ding et al. applied poly(ethylene oxide) (PEO) additive engineering in solution-based film deposition of $Cs_3Sb_2Cl_3I_6$ as an effective defect passivating approach.[25] The resulting devices could charge capacitors, light LEDs, and power small electronics, demonstrating strong potential for the self-powered IoT and wearable energy systems. Further details on this study have been discussed in Section 5 (Defect-Driven Challenges and Mitigation).

Collectively, these studies establish halide substitution as a versatile and powerful approach for engineering dimensionality, the band structure, the charge transport, and intrinsic material stability in Cs–Sb VOPs. The same behavior of phase transition can be observed in Sb-based compounds, upon Br and Cl-substitution in $Cs_3Sb_2I_6$, and band gap narrowing up to

https://doi.org/10.1021/acsomega.6c01559
ACS Omega 2026, 11, 30219–30235

the peak point, which is considered the optimized 2D composition. In particular, the optimized $Cs_3Sb_2Cl_3I_6$ has emerged as one of the most promising state-of-the-art lead-free absorbers for photovoltaics, indoor energy harvesting, photodetection, and self-powered electronic systems, offering a compelling platform for next-generation sustainable optoelectronic technologies.

3.2. Rb-Based VOPs

Rubidium-based halide perovskites have recently attracted significant attention as a new generation of lead-free, all-inorganic perovskite materials with excellent intrinsic material stability and tunable optoelectronic properties. The smaller ionic radius of Rb^+ compared with that of Cs^+ leads to enhanced lattice compactness, reduced defect density, and improved thermal stability, enabling the formation of robust, defect-tolerant perovskite structures.

3.2.1. Bi-Based I/Cl Mixed-Halide Systems. As also demonstrated collectively by Mehmood et al. and McCall et al., halide substitution in Rb−Bi VOPs consistently represents the key lever through which structural symmetry, band-edge energetics, and optoelectronic response have been controlled.[8,10] In the same study of $Cs_3Bi_2I_6Cl_3$by McCall et al., they have investigated the Cl-substitution in $Rb_3Bi_2I_6$. In the Rb-based Bi defect perovskite targeted as $Rb_3Bi_2I_6Cl_3$, site-selective halide distribution is only partial, but it still provides a clear basis for how halide ordering affects the band structure and the transport. Relative to monoclinic $Rb_3Bi_2I_9$ with E_g = 1.93 eV, introducing Cl preferentially into the bridging halide positions slightly widens the gap to 2.02 eV, consistent with a blue shift caused by replacing part of the more electronically coupled Bi−I network with Bi−Cl interactions. Structurally, the smaller Cl^- ions preferentially occupy the bridging sites because they help relax the distorted Rb−Bi bilayer and stabilize a higher-symmetry trigonal framework; however, this ordering is incomplete, so the refined crystal is better described as $Rb_3Bi_2I_5Cl_4$ rather than an ideally ordered $Rb_3Bi_2I_6Cl_3$. Specifically, the bridging site is occupied by about 65% Cl and 35% I, whereas the terminal sites contain about 66% I and 34% Cl, showing that Cl is enriched at bridging positions and I at terminal positions, but not fully segregated as in $Cs_3Bi_2I_6Cl_3$, where the site selectivity is much more distinct.[8] This incomplete ordering in the Rb system likely promotes site mixing, poorer crystallinity, and phase segregation, with the Cl-rich refined composition implying that a complementary I-rich phase remains elsewhere in the melt. Mechanistically, this matters because charge transport is expected to proceed more efficiently through iodide-rich Bi−I−Bi pathways, while Cl in the bridging direction weakens the orbital overlap and therefore increases the anisotropy of carrier transport, especially out-of-plane.

In another study by Mehmood et al., DFT calculations of $Rb_3Bi_2I_6Cl_3$ and $Rb_3Bi_2I_3Cl_6$ were performed using the WIEN2k code under the GGA and TB-mBJ functional method to obtain accurate bandgap values. This comparative analysis demonstrates that the distribution of Cl and I atoms strongly influences their structural, electronic, and optical behavior. Structurally, $Rb_3Bi_2I_6Cl_3$ exhibits higher lattice stability, as reflected by its larger bulk modulus (54.76 GPa) and more negative formation enthalpy (−1.7935 Ry) compared with $Rb_3Bi_2I_3Cl_6$ (44.73 GPa and −0.3269 Ry).[10] The calculation of DOS revealed that the VBM is controlled by I/Cl p orbitals and the CBM is largely composed of Bi 6p orbitals, as shown in Figure 6. The Rb s orbitals have no significant contribution near the Fermi level, pointing to the structural stabilizer

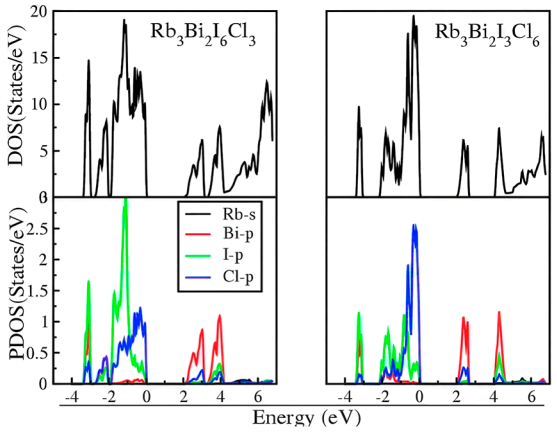

Figure 6. Total DOSs and partial DOSs of the $Rb_3Bi_2I_6Cl_3$ and $Rb_3Bi_2I_3Cl_6$ halide perovskites. Reproduced from ref 10 with permission from the Royal Society of Chemistry.

function of Rb rather than electronic behavior. In terms of electronic properties, both materials are direct band gap semiconductors; however, $Rb_3Bi_2I_3Cl_6$ exhibits a slightly narrower band gap of 1.996 eV compared with 2.061 eV for $Rb_3Bi_2I_6Cl_3$, indicating that halide redistribution modifies the hybridization between Bi-p and halide-p orbitals and enhances visible-light absorption. Carrier transport analysis further shows that $Rb_3Bi_2I_6Cl_3$ possesses lower electron and hole effective masses (0.42 m_e and 1.81 m_e) than $Rb_3Bi_2I_3Cl_6$ (0.73 m_e and 2.30 m_e), suggesting higher carrier mobility in $Rb_3Bi_2I_6Cl_3$. Additionally, $Rb_3Bi_2I_6Cl_3$ exhibits lower exciton binding energies (200.63 and 225.42 meV in X and Z directions) and larger exciton radii (7.47 and 7.05 Å) compared with $Rb_3Bi_2I_3Cl_6$ (363.68 and 305.62 meV; 4.88 and 4.76 Å), indicating easier electron−hole separation and reduced recombination probability. As illustrated in Figure 7, from the optical perspective, $Rb_3Bi_2I_3Cl_6$ shows slightly larger dielectric constants ($\varepsilon_1(0)$ = 5.07 and 4.94 in X and Z directions) and refractive indices ($n(0)$ = 2.25 and 2.22) than $Rb_3Bi_2I_6Cl_3$ ($\varepsilon_1(0)$ = 4.80 and 4.53; $n(0)$ = 2.19 and 2.12), which enhances light−matter interaction and optical absorp-

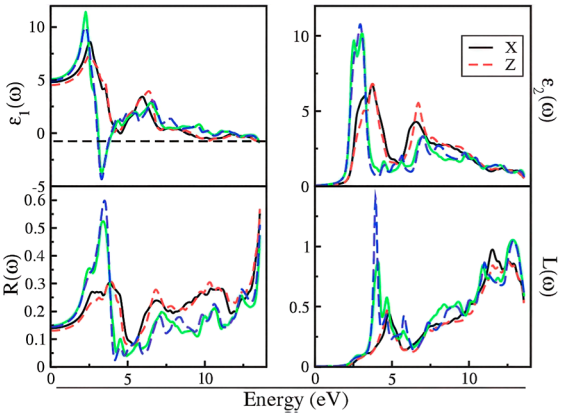

Figure 7. Real (ϵ_1) and imaginary (ϵ_2) parts of dielectric function, reflectivity [$R(\omega)$], and loss function [$L(\omega)$] of the $Rb_3Bi_2I_6Cl_3$ and $Rb_3Bi_2I_3Cl_6$ halide perovskites. Reproduced from ref 10 with permission from the Royal Society of Chemistry.

https://doi.org/10.1021/acsomega.6c01559
ACS Omega 2026, 11, 30219−30235

tion. As a result of this band gap narrowing and improved optical response, the FTO/TiO_2−SnO_2/$Rb_3Bi_2I_6Cl_3$ MoO_3/Ni device achieves a slightly higher simulated photovoltaic efficiency (11.52%) compared with the FTO/TiO_2−SnO_2/$Rb_3Bi_2I_3Cl_6$/MoO_3/Ni device (11.39%), despite $Rb_3Bi_2I_6Cl_3$ showing better carrier transport characteristics. Overall, the Cl/I distribution controls a trade-off between the structural stability and the charge-transport efficiency (favored in $Rb_3Bi_2I_6Cl_3$) and enhanced optical absorption and photovoltaic response (favored in $Rb_3Bi_2I_3Cl_6$), highlighting the importance of halide engineering in tuning the optoelectronic performance of Bi-based 2D perovskites.

3.2.2. Sb-Based Br/I Mixed-Halide Systems. Weber et al. prepared $Rb_3Sb_2Br_{9-x}I_x$ ($x = 0-9$) perovskite series based on a solution-based approach using antisolvent vapor diffusion for single-crystal growth and spin coating with antisolvent dripping for thin-film preparation.[26] Replacing I with the smaller Br ion in $Rb_3Sb_2Br_{9-x}I_x$ continuously compresses the SbX_6 octahedra and reduces the unit-cell volume, yet the material remains a 2D layered monoclinic ($P2_1/n$) crystal structure rather than undergoing a dimensional transition. This structural compression decreases metal-halide orbital overlap and shifts the absorption edge to higher energy, producing a linear bandgap increase from 2.02 eV for $Rb_3Sb_2I_9$ to 2.46 eV for $Rb_3Sb_2Br_9$. At the same time, Br-rich films develop stronger (001) preferential orientation parallel to the substrate, which is unfavorable for out-of-plane charge extraction in a layered material, suppressing carrier transport, lowering EQE, photocurrent, and overall efficiency. Accordingly, the highest-performing iodide-rich device reaches 1.37% PCE, whereas efficiency decreases markedly with increasing Br content. The recombination is also affected, as the PL peak blue-shifts from 639 to 525 nm and PL intensity is much stronger in iodide-rich films, consistent with the changes in radiative/nonradiative pathways. Importantly, $Rb_3Sb_2I_9$-based cells stored in the dark under a nitrogen atmosphere retained 84% of their initial PCE after more than 150 days, with performance measured periodically under 100 mW cm^{-2} illumination, highlighting that iodide-rich compositions provide the best balance of carrier transport, performance, and the device operational stability. Thus, halide chemistry affects performance through coupled changes in the band structure, transport anisotropy, and recombination losses.

Halide substitution in Rb-based mixed-halide perovskites offers a powerful handle to modulate the lattice symmetry, the frontier orbital alignment, and the bandgap energies through controlled tuning of halide p-state contributions. While Cl^- and Br^- incorporation enhances structural robustness and stabilizes higher-symmetry layered frameworks, iodine-rich compositions maintain stronger visible absorption and more favorable electronic coupling. These trends collectively highlight halide engineering as a key design principle for advancing stable lead-free perovskite absorbers with tunable optoelectronic functionality.

4. DEFECT-DRIVEN CHALLENGES AND MITIGATION

Halide alloying is an effective approach to passivating the defects in $A_3B_2X_9$ VOP materials. However, as reported in the literature, these mixed-halide VOPs are also suffering from defect-induced carrier recombination, which ultimately reduces the performance of the optoelectronic devices. In compounds such as $Cs_3Bi_2I_6Cl_3$, a major recombination pathway is associated with STEs, which are identified from broad, strongly temperature-dependent PL and its agreement with Raman-active phonons, evidencing a highly lattice-coupled excited state. The Jahn−Teller distortion, X-site halide disorder associated with the antisite defects [I_{Cl} (I-on-Cl) and Cl_I (Cl-on-I)], and a low dimension are responsible for STE formation. Compared with 3D lead-halide perovskites and even some double perovskites, this compound shows much stronger electron−phonon coupling, favoring small-polaron formation and carrier localization. As a result, recombination is dominated by phonon-assisted STE emission, which broadens luminescence but generally reduces the carrier mobility, the diffusion length, and the device efficiency.[8,28]

Several techniques are used to diagnose defect- and trap-mediated losses in $A_3B_2X_9$-type materials. Time-resolved photoluminescence (TRPL) is commonly employed to probe trap-assisted recombination through carrier-decay dynamics; nanosecond lifetimes, as reported for $Cs_3Sb_2I_9$, generally indicate high trap densities, whereas microsecond lifetimes in $A_3Bi_2I_9$ single crystals suggest fewer active nonradiative centers.[29,30] Transient absorption spectroscopy provides further insight into carrier persistence and excited-state evolution after photoexcitation.[31] Deep-level transient spectroscopy and photoinduced current transient spectroscopy (PICTS) are particularly useful for identifying the energetic positions of deep traps, including defect levels reported at 0.41 eV in $Cs_3Sb_2I_9$ and 0.62 eV in $Rb_3Sb_2I_9$.[32] UPS/XPS helps determine the Fermi-level position, band alignment, and possible Fermi-level pinning by self-compensating defects.[33] In addition, temperature-dependent conductivity and space-charge-limited current (SCLC) measurements are widely used to evaluate activation energies, conduction mechanisms, and trap densities in polycrystalline films.[34]

Additive engineering with poly(ethylene oxide) (PEO) has been reported as an effective strategy for defect passivation, crystal growth modulation, and enhancement of film quality in $Cs_3Sb_2Cl_3I_6$-based triboelectric nanogenerators (TENGs).[25] PEO acts as a ligand modifier that passivates both interface and bulk lattice defects, yielding denser, pinhole-free films. The mechanism involves the ether bond (C−O−C) in the PEO structure; specifically, the oxygen atoms provide electrons to form a coordination interaction with Sb^{3+} ions. This suppression of uncoordinated defect sites significantly reduces nonradiative recombination, which is evidenced by an increase in photoluminescence (PL) intensity and a prolongation of the average carrier decay lifetime from 2.95 to 11.14 ns. Dielectric constant also improved, permitting greater charge storage capacity. Consequently, the modified device exhibited markedly improved optoelectronic−triboelectric coupled output, with the open-circuit voltage and short-circuit current increasing to 184 V and 19.1 μA, respectively, along with a maximum power density of 2.13 W m^{-2} and excellent long-term operation stability of the device, which can maintain 90.9% of its initial triboelectric output within 40 days and full functionality after 5000 operation cycles.[25] Several defect mitigation strategies have been reported for VOPs, including A-site cation mixing, treating the VOPs with ligands, increasing grain sizes, and alternative charge transport layers, which may also be applicable to mixed-halide VOP systems. According to those reports, incorporating MA or FA at the A-site is suggested to improve the film density, reduce dark current, and further minimize the nonradiative recombination in Cs-Bi-based films. Moreover, treating the VOPs with ligands such as oleylamine, oleate, or octylammonium halides is also a

https://doi.org/10.1021/acsomega.6c01559
ACS Omega 2026, 11, 30219−30235

recommended strategy, which has been proven to passivate defects and has been shown to improve photoluminescence quantum yields (PLQYs) in $Cs_3Bi_2Br_9$. A viable defect-mitigation strategy is to reduce the grain-boundary density, since grain boundaries act as the nonradiative recombination centers and ion-migration pathways. This has been achieved through increasing the grain size via improved film thickness. A wide range of other approaches have also been adopted (both for VOPs and more generally for thin film semiconductors), including hot casting and postsynthetic vapor annealings.[33]

The selection of charge transport layers is a critical component of defect mitigation in VOPs, as these layers can directly passivate surface traps and improve the charge extraction efficiency before recombination occurs. For instance, $Cs_3Sb_2I_9$-based PSCs, substituting traditional Spiro-OMeTAD with P3HT, have been shown to improve charge extraction as its valence band aligns well with the active absorber layer, resulting in suppression of the dark current and facilitating rapid charge extraction. Sensitization of the ETLs is an effective device-engineering strategy to enhance performance by facilitating electron extraction, improving energy-level alignment, reducing interfacial defects, and increasing light harvesting. For example, chlorophyll-derivative sensitization of TiO_2 (ETL) improved PCE by reducing the defects and suppressing interfacial recombination.[35] Overall, these results indicate that effective defect mitigation in mixed-halide VOPs requires a combined strategy involving chemical passivation, grain-boundary control, and transport-layer/interface engineering to suppress the nonradiative recombination and enable more efficient and stable devices.

5. SYNTHESIS ROUTES

5.1. Radio Frequency Magnetron Sputtering

The RF magnetron sputtering technique is a vacuum-based deposition for fabricating mixed-halide perovskite thin films in which target composition, the RF power, air pressure, the target−substrate distance, the film thickness, and the post-annealing process become the main variables governing the phase formation and microstructure. In this process, pressed powder targets containing halide precursors are sputtered onto precleaned glass or conductive substrates under an argon plasma atmosphere. Bonami et al. followed this technique for the first time using CsBr, CsI, BiI_3, and $BiBr_3$ precursors to synthesize the $Cs_3Bi_2(I_{1-x}Br_x)_9$ $(0 \leq x \leq 1)$ series. In their process, they have utilized an RF power of 40−100 W, an argon pressure of 2×10^{-2} mbar, and a target−substrate distance of 10 cm. The resulting films are then vacuum annealed at 200 °C to enhance crystallinity and the compositional homogeneity. The study proved that the RF sputtering technique delivers high-quality single-phase mixed-halide VOP films, indicating narrow diffraction peaks and Raman line widths close to single-crystal values, while the mixed-halide films exhibited Br/I ratios close to the nominal target composition, with deviations of only about ±5%.[6] This method uses a single target source, which allows for excellent stoichiometry control, leading to the production of high-quality, single-phase crystalline films for alloyed compositions. When comparing the solution-based methods, such as the spin coating, this process effectively circumvents the "dissolution problems" and associated complications. In this sense, sputtering offers a trade-off: phase purity and reproducibility are generally better than in solution routes because the solvent retention, the nonuniform drying, and the ambient-induced variability are avoided, and dry deposition is inherently compatible with the large-area manufacturing and texture substrates. Furthermore, sputtering provides very good substrate coverage, resulting in films with high crystallinity and good morphology, which is achieved through careful optimization of composition and plasma conditions.[36] Consequently, the efficiency of light absorption and charge transport within the perovskite layer is enhanced, leading to improved device performance. Moreover, sputtering is a scalable deposition technique suitable for large-area production, and its cost-effectiveness is further emphasized by its lower consumption of source material compared to other methods.[37] On the other hand, the post-annealing process may be considered a minor drawback, since it is compulsory to achieve high crystallinity. Overall, this solvent-free technique offers high film quality, smooth morphology, and excellent phase control, which is confirmed by structural, morphological, and optical property characterization, making it a promising and scalable route for lead-free, all-inorganic perovskite optoelectronic applications.[6]

5.2. The Solution-Based Spin-Coating Method

The solution-based spin-coating technique is a widely used approach for fabricating mixed-halide perovskite thin films with excellent compositional control and uniformity. In this process, halide precursors such as CsI, SbI_3, and $SbCl_3$ are dissolved in a dimethyl sulfoxide (DMSO)/dimethylformamide (DMF) (3:1) solvent mixture and stirred overnight at 70 °C to ensure homogeneity. The filtered solution is then spin-coated at 4000 rpm for 30 s, while toluene is introduced as an antisolvent to promote rapid crystallization. Postdeposition, the films are annealed at 100−150 °C for 30 min, often under solvent-vapor conditions using DMSO, which enhances crystallinity and surface morphology. This reproducible, low-temperature process yields high-quality, lead-free $Cs_3Sb_2Cl_xI_{9-x}$ thin films, ideal for optoelectronic and photovoltaic applications. Penga et al. adopted this method to deposit $Cs_3Sb_2Cl_xI_{9-x}$.[13] Yu has followed the same process to synthesize thin films of the $Cs_3Bi_2I_{9-x}Br_x$ series.[16]

Ding et al. developed a modified solution-processing method to enhance the structural and electronic quality of $Cs_3Sb_2Cl_3I_6$ thin films.[25] Unlike conventional procedures, this route employed a DMF/DMSO solvent ratio of 1:3 to slow solvent evaporation and improve the film uniformity. Poly(ethylene oxide) (PEO) was incorporated (0−10 mg mL^{-1}) as an additive to regulate crystallization and passivate surface defects. The films were deposited on ITO substrates, pretreated by ethanol/isopropanol sonication and UV−ozone exposure to improve the surface energy and adhesion. A two-step spin-coating process (500 rpm for 10 s, then 2000 rpm for 30 s) replaced the single-step method, enabling smoother, more compact layers. Finally, annealing at 135 °C for 30 min yielded highly uniform films with enhanced crystallinity, reduced trap density, and improved optoelectronic performance.

The advantages of the solution-based spin-coating process lie in the fact that it is beneficial for the optimization of the process on a laboratory scale at low cost without advanced equipment setups. The main disadvantage of the spin-coating process is that the phase purity of the material is highly dependent on the concentration of the precursors, the spin speed, the acceleration, the drying rate, and the thermal history. The high drying rate of the solvent leads to setting the

https://doi.org/10.1021/acsomega.6c01559
ACS Omega 2026, 11, 30219−30235

film in a short time, which may not be the most stable configuration of the material. The spin-coating process is beneficial for the medium-scale modules, but the disadvantage of the process is that the material utilization efficiency is extremely low. The spin-coating process is not beneficial for large-scale modules due to the difficulty in maintaining the uniformity of the process. The process parameters affect the nucleation and grain growth of the material, thereby affecting the efficiency of the solar cells.

5.3. Mechanochemical Solid-State Synthesis

Giovilli developed a mechanochemical solid-state synthesis method to prepare mixed-halide perovskites such as $Cs_3(Sb_{1-x}Bi_x)_2Br_9$ and $Cs_3Sb_2(Br_{1-x}I_x)_9$ in a solvent-free and environmentally friendly manner.[14] This study is the first mechanochemical synthesis of the layered polymorph of the $Cs_3Sb_2I_9$ perovskite, previously obtained only via a conventional solid-state reaction. Stoichiometric amounts of precursor powders (CsBr, $SbBr_3$, $BiBr_3$ or CsI, $SbBr_3$, SbI_3) were mixed and loaded into a tungsten carbide (WC) planetary grinding bowl with WC balls at a 10:1 ball-to-powder ratio. Grinding was performed using a Planetary Micro Mill, applying repeated grinding−pause cycles to promote solid-state reactions. For the bi-substituted series, six cycles at 400 rpm were used, while the halide-substituted series required ten cycles at 600 rpm for the complete homogenization.

Mechanochemical solid-state synthesis is a viable alternative method to overcome the solubility issues of halide precursors faced by traditional solution-based syntheses. Consequently, the process is highly effective for producing single-phase materials for complex mixed compositions, such as Sb/Bi and Br/I systems, ensuring full solubility of the lattice. Furthermore, this technique is reliable for preserving the intended stoichiometries of both pure and alloyed samples. However, unlike solution-chemistry synthesis methods, mechanochemically prepared samples do not possess a well-defined morphology, as observed by Giovilli et al.[14] The resulting materials consisted of grains with various shapes and dimensions, typically ranging from the micrometer to submicrometer scale, which may increase the grain-boundary density and the defect-assisted recombination if such powders are translated into optoelectronic films. Moreover, the process highly depends on milling parameters such as the number of cycles, milling time, and rotational speed. Careful optimization of these parameters is required to obtain the phase-pure samples. Otherwise, they can result in mixed-phase samples containing unwanted polymorphs. Despite these limitations, the mechanochemical synthesis method offers the key benefit of enabling solvent-free, energy-efficient, and environmentally friendly production of phase-pure perovskite materials, with excellent compositional control and uniformity, provided that the process parameters are carefully optimized.

5.4. Solution-Based Antisolvent Vapor Diffusion Crystallization Method

In a study by Weber et al., single crystals of $Rb_3Sb_2Br_{9-x}I_x$ were prepared by a solution-based antisolvent vapor diffusion crystallization technique. Stoichiometric amounts of SbI_3, $SbBr_3$, RbI, and RbBr were dissolved in DMF and stirred at 70 °C under nitrogen to form a homogeneous precursor solution. Then, slowly evaporating an antisolvent (such as dichloromethane or chloroform) was allowed to diffuse into the precursor solution to gradually reduce solubility and cause controlled precipitation of single crystals over several days. The method is effective for the preparation of perovskite films by adopting the vapor diffusion crystallization method during spin-coating the perovskite precursor solution on the substrate. As determined by Weber et al., this slow-diffusion process allows for the formation of high-quality, well-faceted monoclinic layered crystals suitable for detailed structural and optoelectronic characterization.[26] In addition to that, perovskite films with pure and stable crystal phases with excellent surface coverages can be prepared, leading to highly reproducible efficiencies. The slow process promotes stoichiometric growth of high-quality single crystals with very low trap densities, which are beneficial for the charge transport.

However, unlike rapid thin-film deposition, this method is time-consuming, requiring several days for the antisolvent to evaporate and condense the precursor solution to precipitation. Importantly, the final crystal quality strongly depends on the nature of the antisolvent, the solvent/antisolvent volume ratio, the exact timing of diffusion, the temperature, and the diffusion rate. A poorer antisolvent lowers solubility more effectively, while slower vapor diffusion favors crystal growth over excessive nucleation. Therefore, careful optimization of these parameters is essential to obtain dense, uniform films with improved morphology and enhanced optoelectronic performance.[38]

5.5. Two-Step Solvent Evaporation Method

Manuel Daum et al. synthesized $Cs_3Bi_2Br_3I_6$ wafers using a two-step solvent evaporation and pellet pressing method. Initially, CsBr (6 mmol) and BiI_3 (3 mmol) were dissolved in a DMF/DMSO (4:1) solvent mixture and filtered to form a clear dark red precursor solution. The solution was evaporated at 160 °C, producing small crystalline solids, which were subsequently washed with ethanol and dried overnight at 60 °C to obtain fine red-violet crystallites.[27] These crystallites were ball-milled into a uniform powder and then pressed into dense wafers using a 13 mm pellet die under 0.3 GPa for 30 min, yielding 0.7 mm-thick pellets. The resulting wafers retained optical properties similar to thin films, exhibiting a direct band gap near 620 nm with a strong absorption onset typical of semiconductor behavior.

Even though this combined synthesis route offers a useful compromise between the solution processability and the dense bulk device fabrication, it introduces several important trade-offs. Its tendency to produce compact, phase-rich wafers with good optical absorption and mechanical robustness is a major advantage. This method excels in scalability, as the pellet-pressing supports gram-scale outputs suitable for industrial translation, and offers good reproducibility through controlled evaporation rates and uniaxial pressing parameters, minimizing batch-to-batch variability compared to the solution-casting alone. However, trade-offs emerge in the phase purity, where the rapid evaporation risks incomplete halide mixings, potentially yielding secondary phases in iodide-rich systems, while pellet pressing can induce microstrains, necessitating a post-processing optimization. Processing variables directly affect microstructure: slower, controlled crystallization, and better powder homogenization generally increase the grain size and reduce the grain-boundary defect density, whereas rapid evaporation, insufficient compaction, or residual solvents can increase the trap density, carrier scattering, dark current instability, and ultimately degrade the detector sensitivity (in the case of photodetectors) and charge-transport performance. This method differs from conventional spin-coating by

https://doi.org/10.1021/acsomega.6c01559
ACS Omega 2026, 11, 30219−30235

producing dense, phase-pure bulk perovskites with stable optical and electronic properties, ideal for X-ray detection and optoelectronic characterization.

5.6. Sealed-Tube Melt Synthesis (Ampule Method) and Bridgman Synthesis

Kyle M. McCall et al. employed sealed-tube melt synthesis (ampule method) to obtain bulk $A_3Bi_2I_6Cl_3$ (A = Cs, Rb) with high phase purity and crystallinity.[8] Stoichiometric ACl and BiI_3 powders (e.g., 4.5 mmol ACl and 3 mmol BiI_3) are thoroughly mixed, loaded into a fused-silica ampule (10 mm o.d.), evacuated to 3×10^{-3} mbar, flame-sealed, and heated in a tube furnace to 750 °C (10 h ramp), held 10 h, then cooled 10 h to solidify the melt. The process yields dark cherry-red polycrystalline ingots; 1 mm single crystals can be obtained by cleaving along lamellar planes. The products are air-stable but hydrolytically sensitive (decompose in water over hours). For example, $Cs_3Bi_2I_6Cl_3$ single crystals were grown by vertical Bridgman synthesis from stoichiometric CsCl and BiI_3 sealed under vacuum in a pointed ampule. After complete melting at 725 °C for 12 h, the ampule was lowered at 1 mm h^{-1}, annealed at 300 °C, and slowly cooled, yielding large, easily cleavable crystals.

The main advantages of this process are the high-temperature controllability, controllable vessel geometry, and the ability to grow crystals from a homogeneous melt in a sealed environment. Because the precursors are melted above their melting point and recrystallized under a defined thermal gradient, the method can promote good phase purity by improving precursor intermixing and suppressing volatilization or contamination. It is mostly recommended for mixed-halide compositions since the halide ratio in the final crystal can, in principle, track the precursor ratio when the melt remains chemically homogeneous. The slow directional solidification usually lowers the nucleation density, producing larger grains or single-crystal domains, which reduces grain-boundary-related traps and improves carrier transport, lifetime, and therefore detector or photovoltaic performance.

The main limitations arise from the thermal and interfacial instability. If the temperature is too high, fluctuates, or the furnace position is not optimized, the solid−liquid interface becomes unstable, and inclusions can form. Consequently, secondary phases, local halide segregations, or incomplete halide orderings may occur, especially in mixed-halide systems where different halides may redistribute during the melt equilibration and cooling. Reproducibility depends strongly on the precisely controlled melt temperature, soak time, cooling rate, and ampule geometry; small deviations can change the interface curvature and the defect density. The scalability is possible for large boules, but is constrained by the vessel size, long crystal growth times, and wall-induced stress. Contact with the ampule wall can generate cracks, subgrain boundaries, and residual strain, which increase the trap density, enhance nonradiative recombination, and degrade the carrier mobility, dark current, and overall device stability and performance.[39] Compared with solution or sputtering routes, this method provides a bulk reference material ideal for single-crystal/phase analysis and intrinsic property measurements.[8]

Overall, these synthesis techniques enable consistent control over the composition, phase purity, and film morphology.

6. PATHWAYS TO HIGHER STABILITY AND EFFICIENCY IN LEAD-FREE MIXED-HALIDE VOPS

Even though lead-free mixed halide perovskites demonstrate enhanced efficiency and environmental stability compared to other types of VOPs, further enhancements are essential for the successful large-scale commercialization. Therefore, novel strategies are necessary to enhance the performance and operational stability of the device further. In our view, the main factors limiting efficiency and stability are the defect-mediated nonradiative recombination, the self-trapping of charge carriers, interfacial charge-extraction losses, the incomplete control over phase purity and the halide distribution, and the environmental degradation under heat, moisture, and prolonged operation. These constraints are interrelated; poor crystallization or compositional inhomogeneity increases defect density, which, in turn, enhances the carrier localization and accelerates the degradation pathways.

The performance improvements can be achieved through several strategies, including the incorporation of additives, surface passivation, the use of alternative charge transport materials, and the enhancement of film quality through advanced film fabrication processes. Incorporation of photosensitizers and dyes in the PSCs may be a suitable way to tune the optical properties and enhance the performance as they can broaden optical absorption in the UV region, facilitate efficient charge migrations, and enhance long-term stability. To enhance the absorption coefficient and band gap tuning, the addition of reducing agents and additives might be an effective approach. From a device-engineering perspective, alternative charge-transport materials beyond conventional ETLs and HTLs may offer better band alignment, lower interfacial recombinations, and improved chemical compatibility with mixed-halide VOP absorbers. Combining the solution and vapor-based deposition methods is an effective strategy to get a high-quality film, minimizing the defect density, controlling the grain size and structural dimensionality, and leading to high-performance optoelectronic devices. Hybrid metal halide PSCs have gained significant attention recently as highly promising candidates for multijunction tandem solar cells, exceeding the PCE of 26%. In this context, the mixed-halide VOP materials represent a potential class of absorber materials for tandem photovoltaics architectures. These materials can be used as standalone absorbers in all-perovskite tandem devices or as top-cell absorbers when integrated with other photovoltaic technologies. Their suitability arises from their tunable band gap, which falls within the desirable range of 1.17−2.23 eV for efficient tandem solar cells.

The mixed-halide VOPs and the optoelectronic devices already demonstrate higher environmental stability compared to their counterparts.[13,16] Those materials' intrinsic stability can be further improved by B-site (Bi^{3+}/Sb^{3+}) alloying, as it can enhance the lattice stability and suppress the structural distortions. Mixed B-site compositions such as $Cs_3(Sb_xBi_{2-x})X_9$ can reduce the defect formation energy and stabilize the crystal structure, which enhances the environmental and thermal stabilities. Surface defects and halide vacancies can accelerate the degradation. Surface passivation using organic ligands, ammonium salts, or polymer layers can reduce trap states, suppress ion migrations, and improve both the stability and the device performance. In this context, the long-term success of mixed-halide VOPs will depend on whether future research can simultaneously address the stability, the defect tolerance, and

https://doi.org/10.1021/acsomega.6c01559
ACS Omega 2026, 11, 30219−30235

the charge-transport efficiency in a unified material-design framework.

7. CONCLUSION AND FUTURE OUTLOOK

Lead-free mixed halide-based VOPs, which belong to the $A_3B_2X_9$ family, are an emerging class of materials for the replacement of toxic Pb-based counterparts. Importantly, halide alloying (Cl/Br/I) facilitates the control of dimensionality (0D to 2D), symmetry, band edge energetics, excitonic behavior, and intrinsic material stability. When considering halide perovskites, iodide-rich compositions typically stabilize 0D dimeric structures with indirect or weakly allowed transitions and strong carrier localization, which restricts photocurrent generation. Partial substitution with smaller halides (Cl^- or Br^-) contracts the lattice, improves octahedral connectivity, and frequently converts the 0D structure to a 2D layered phase, enhancing the orbital overlap and band dispersion. Consequently, mixed-halide VOPs often show direct or quasi-direct band gaps, reduced exciton binding energies, and enhanced carrier transport.

Overall, reported band gaps span a wide range of 1.7−2.8 eV, while optimized layered compositions cluster around 1.9−2.1 eV, making them particularly attractive for visible-light photovoltaics, indoor PV, photodetectors, and tandem solar cells. Halide alloying also has a remarkable impact on film quality, long-term operational stability, and performance of the optoelectronic devices. Mixed-halide thin films generally show larger grains, improved surface coverage, reduced trap densities, and improved crystallinity, resulting in higher performance and excellent intrinsic material stability relative to their single-halide counterparts. A wide range of synthesis routes, comprising solution-based spin coating with antisolvent engineering, RF magnetron sputtering, mechanochemical solid-state synthesis, sealed-tube melt growth, wafer pressing, and vapor-diffusion crystallization, have been exhibited, enabling control over the phase purity, composition, and morphology from thin films to bulk crystals.

Future development should prioritize (i) comparative theoretical (integrating first-principles calculations) and device level modeling on different halide-alloying schemes, together with detailed theoretical and experimental studies on Rb-based VOPs, (ii) precise control of halide homogeneity near phase-transition regimes, (iii) defect chemistry mapping and improved passivation strategies, (iv) interface and band-alignment engineering (different HTL and ETL combinations) for efficient charge extraction and improved performance, and (v) comprehensive long-term operational stability investigation of the devices under realistic environmental stressors. With these advances, mixed-halide VOPs are well-positioned to evolve from promising lead-free alternatives into application-ready optoelectronic semiconductors.

For readers seeking a useful entry point into this topic, several representative studies deserve particular attention. Early foundational reports established the structural chemistry and vacancy-ordered framework of these materials.[8,11,12] Subsequent studies clarified the effect of halide alloying in VOPs and site-selective occupancy of the alloyed halide on the band structure, optoelectronic properties, and recombination behavior.[7−11,13,14,16] More recent reports have addressed defect passivation, stability improvement, numerical simulation-based performance prediction, and novel applications of mixed-halide VOPs.[7,10,33,35]

AUTHOR INFORMATION

Corresponding Author

Galhenage A. Sewvandi − *Department of Materials Science and Engineering, Faculty of Engineering, University of Moratuwa, Moratuwa 10400, Sri Lanka;* orcid.org/0000-0002-2994-9063; Email: galhenagea@uom.lk

Author

Walagedara G. A. Pabasara − *Department of Materials Science and Engineering, Faculty of Engineering, University of Moratuwa, Moratuwa 10400, Sri Lanka; Department of Engineering Technology, Faculty of Technology, University of Ruhuna, Uyangoda, Kamburupitiya 81100, Sri Lanka;* orcid.org/0000-0002-2340-2219

Complete contact information is available at: https://pubs.acs.org/10.1021/acsomega.6c01559

Notes

The authors declare no competing financial interest.

Biography

Eng. Walagedara G.A. Pabasara earned her Bachelor of Science in Engineering in Materials Science and Engineering from the Faculty of Engineering, University of Moratuwa, Sri Lanka, in 2017, where she is now pursuing her Ph.D. in the same discipline. She currently serves as a Lecturer attached to the Department of Engineering Technology, University of Ruhuna, Sri Lanka. Her research focuses on perovskite solar cells, particularly on enhancing their stability and reducing toxicity to improve their potential for practical applications. Her work mainly involves computational simulations and machine learning approaches for the compositional engineering of perovskite materials, aiming to optimize their performance and promote the development of efficient, stable, and environmentally sustainable solar cell technologies.

Galhenage A. Sewvandi is a Professor in Materials Science and Engineering at the University of Moratuwa, Sri Lanka. She obtained her Ph.D. in Advanced Materials from Kagawa University, Japan, in 2015. Her research interests include advanced functional materials, perovskite solar cells, and machine learning-assisted materials discovery. She has made significant contributions to the development of lead-free perovskite materials for sustainable energy applications.

ACKNOWLEDGMENTS

The authors sincerely thank the Department of Materials Science and Engineering, Faculty of Engineering, University of Moratuwa, for providing the facilities and support for this research.

REFERENCES

(1) Jayawardane, S. T.; Akmal, M. D.; Jayaneththi, Y. H.; Fernando, T. V.; Hu, D.; Abeygunawardhana, P. K. W.; Sewvandi, G. A. Simulation-Based Performance Analysis of Lead-Free Bismuth Perovskite Solar Cells: A Comparative Study of $Cs_3Bi_2I_9$ and $(CH_3NH_3)_3Bi_2I_9$ -Based Perovskite Solar Cells. *Adv. Theory Simul.* **2024**, *7* (7), 2400206.

(2) Sanjeewani Thakshila Jayawardane, J. T.; Don Muditha Akmal, U. K.; Hu, D.; Wijesekara Abeygunawardhana, P. K.; Sewvandi, G. A. Eco-Friendly Bismuth Halide Chalcogenide Perovskites for Solar Energy Harvesting. *Sustain. Energy Fuels* **2025**, *9* (8), 2197−2206.

(3) Pabasara, W. G. A.; Akmal, U. K. D. M.; Sewvandi, G. A. Simulation-Guided Investigation of the Effect of 2D Perovskites on

Performances of 2D/3D Mixed Dimensional Perovskite Solar Cells. *Next Energy* **2025**, *9*, 100467.
(4) Pabasara, W. G. A.; Wijerathne, H. A. H. M.; Karunarathne, M. G. M. M.; Sandaru, D. M. C.; Abeygunawardhana, P. K. W.; Sewvandi, G. A. Exploring Nontoxic Perovskite Materials for Perovskite Solar Cells Using Machine Learning. *Discovery Mater.* **2025**, *5* (1), 123.
(5) Pradhan, A.; Jena, M. K.; Samal, S. L. Understanding of the Band Gap Transition in $Cs_3Sb_2Cl_{9-X}Br_x$: Anion Site Preference-Induced Structural Distortion. *ACS Appl. Energy Mater.* **2022**, *5* (6), 6952−6961.
(6) Bonomi, S.; Galinetto, P.; Patrini, M.; Romani, L.; Malavasi, L. Optical and Structural Property Tuning in Physical Vapor Deposited Bismuth Halides $Cs_3Bi_2(I_{1-X}Br_x)_9$ ($0 \leq x \leq 1$). *Inorg. Chem.* **2021**, *60* (18), 14142−14150.
(7) Mehmood, S.; Ali, Z.; Khan, S. R.; Alanazi, M. M.; Abdelmohsen, S. A. M.; Mousa, M. Improving Optoelectronic and Solar Cell Performance from 24 to 31% via Switching from 0D $Cs_3Bi_2I_9$ to 2D $Cs_3Bi_2I_6Cl_3$ Perovskite for Energy Harvesting Application. *Comput. Condens. Matter* **2025**, *44*, No. e01059.
(8) McCall, K. M.; Stoumpos, C. C.; Kontsevoi, O. Y.; Alexander, G. C. B.; Wessels, B. W.; Kanatzidis, M. G. From 0D $Cs_3Bi_2I_9$ to 2D $Cs_3Bi_2I_6Cl_3$: Dimensional Expansion Induces a Direct Band Gap but Enhances Electron-Phonon Coupling. *Chem. Mater.* **2019**, *31* (7), 2644−2650.
(9) Morgan, E. E.; Mao, L.; Teicher, S. M. L.; Wu, G.; Seshadri, R. Tunable Perovskite-Derived Bismuth Halides: $Cs_3Bi_2(Cl_{1-x}I_x)_9$. *Inorg. Chem.* **2020**, *59* (6), 3387−3393.
(10) Mehmood, S.; Ali, Z.; Khan, S. R.; Alanazi, M. M.; Abdelmohsen, S. A. M.; Mousa, M. Unveiling 2D $Rb_3Bi_2I_6Cl_3$ and $Rb_3Bi_2I_3Cl_6$ Perovskites for Optoelectronic, Solar Cell and Photocatalytic Applications. *RSC Adv.* **2025**, *15* (22), 17420−17434.
(11) Aslam, S.; Farooqi, A. S.; Rahman, M. Y. A.; Samsuri, S. A. M. Titanium-Based Vacancy-Ordered Double Halide Family in Perovskite Solar Cells. *Phys. Status Solidi* **2022**, *219* (8), 2100671.
(12) Murugan, S.; Lee, E.-C. Recent Advances in the Synthesis and Application of Vacancy-Ordered Halide Double Perovskite Materials for Solar Cells: A Promising Alternative to Lead-Based Perovskites. *Materials (Basel)* **2023**, *16* (15), 5275.
(13) Peng, Y.; Li, F.; Wang, Y.; Li, Y.; Hoye, R. L. Z.; Feng, L.; Xia, K.; Pecunia, V. Enhanced Photoconversion Efficiency in Cesium-Antimony-Halide Perovskite Derivatives by Tuning Crystallographic Dimensionality. *Appl. Mater. Today* **2020**, *19*, 100637.
(14) Giovilli, G.; Albini, B.; Grisci, V.; Bonomi, S.; Moroni, M.; Mosconi, E.; Kaiser, W.; De Angelis, F.; Galinetto, P.; Malavasi, L. Band Gap Tuning through Cation and Halide Alloying in Mechanochemically Synthesized $Cs_3(Sb_{1-x}Bi_x)_2Br_9$ and $Cs_3Sb_2(I_{1-x}Br_x)_9$ Solid Solutions. *J. Mater. Chem. C* **2023**, *11* (30), 10282−10291.
(15) Shin, S. S.; Correa Baena, J. P.; Kurchin, R. C.; Polizzotti, A.; Yoo, J. J.; Wieghold, S.; Bawendi, M. G.; Buonassisi, T. Solvent-Engineering Method to Deposit Compact Bismuth-Based Thin Films: Mechanism and Application to Photovoltaics. *Chem. Mater.* **2018**, *30* (2), 336−343.
(16) Yu, B. B.; Liao, M.; Yang, J.; Chen, W.; Zhu, Y.; Zhang, X.; Duan, T.; Yao, W.; Wei, S. H.; He, Z. Alloy-Induced Phase Transition and Enhanced Photovoltaic Performance: The Case of $Cs_3Bi_2I_{9-x}Br_x$ Perovskite Solar Cells. *J. Mater. Chem. A* **2019**, *7* (15), 8818−8825.
(17) Steele, J. A.; Puech, P.; Keshavarz, M.; Yang, R.; Banerjee, S.; Debroye, E.; Kim, C. W.; Yuan, H.; Heo, N. H.; Vanacken, J.; Walsh, A.; Hofkens, J.; Roeffaers, M. B. J. Giant Electron-Phonon Coupling and Deep Conduction Band Resonance in Metal Halide Double Perovskite. *ACS Nano* **2018**, *12* (8), 8081−8090.
(18) Ni, C.; Hedley, G.; Payne, J.; Svrcek, V.; McDonald, C.; Jagadamma, L. K.; Edwards, P.; Martin, R.; Jain, G.; Carolan, D.; Mariotti, D.; Maguire, P.; Samuel, I.; Irvine, J. Charge Carrier Localised in Zero-Dimensional $(CH_3NH_3)_3Bi_2I_9$ Clusters. *Nat. Commun.* **2017**, *8* (1), 1−7.
(19) Liu, D.; Yu, B.-B.; Liao, M.; Jin, Z.; Zhou, L.; Zhang, X.; Wang, F.; He, H.; Gatti, T.; He, Z. Self-Powered and Broadband Lead-Free Inorganic Perovskite Photodetector with High Stability. *ACS Appl. Mater. Interfaces* **2020**, *12* (27), 30530−30537.
(20) Peng, Y.; Huq, T. N.; Mei, J.; Portilla, L.; Jagt, R. A.; Occhipinti, L. G.; MacManus-Driscoll, J. L.; Hoye, R. L. Z.; Pecunia, V. Lead-Free Perovskite-Inspired Absorbers for Indoor Photovoltaics. *Adv. Energy Mater.* **2021**, *11* (1), 2002761.
(21) Mathews, I.; Kantareddy, S. N.; Buonassisi, T.; Peters, I. M. Technology and Market Perspective for Indoor Photovoltaic Cells. *Joule* **2019**, *3* (6), 1415−1426.
(22) Pecunia, V. Efficiency and Spectral Performance of Narrow-band Organic and Perovskite Photodetectors: A Cross-Sectional Review. *J. Phys. Mater.* **2019**, *2* (4), 042001.
(23) Azimi, H.; Ameri, T.; Zhang, H.; Hou, Y.; Quiroz, C. O. R.; Min, J.; Hu, M.; Zhang, Z.-G.; Przybilla, T.; Matt, G. J.; Spiecker, E.; Li, Y.; Brabec, C. J. A Universal Interface Layer Based on an Amine-Functionalized Fullerene Derivative with Dual Functionality for Efficient Solution Processed Organic and Perovskite Solar Cells. *Adv. Energy Mater.* **2015**, *5* (8), 1401692.
(24) Cotfas, D. T.; Cotfas, P. A. Multiconcept Methods to Enhance Photovoltaic System Efficiency. *Int. J. Photoenergy* **2019**, *2019* (1), 1905041.
(25) Ding, L.; Wei, Z.; Zeng, X.-Y.; Fang, K.; Wang, G.-G. Lead-Free Perovskite $Cs_3Sb_2Cl_3I_6$ via Additive Engineering for Enhancing Output Performance of Optoelectronic and Triboelectric Coupled Nanogenerator. *Nano Energy* **2025**, *133*, 110451.
(26) Weber, S.; Rath, T.; Fellner, K.; Fischer, R.; Resel, R.; Kunert, B.; Dimopoulos, T.; Steinegger, A.; Trimmel, G. Influence of the Iodide to Bromide Ratio on Crystallographic and Optoelectronic Properties of Rubidium Antimony Halide Perovskites. *ACS Appl. Energy Mater.* **2019**, *2* (1), 539−547.
(27) Daum, M.; Deumel, S.; Sytnyk, M.; Afify, H. A.; Hock, R.; Eigen, A.; Zhao, B.; Halik, M.; These, A.; Matt, G. J.; Brabec, C. J.; Tedde, S. F.; Heiss, W. Self-Healing $Cs_3Bi_2Br_3I_6$ Perovskite Wafers for X-Ray Detection. *Adv. Funct. Mater.* **2021**, *31* (47), 2102713.
(28) Zhang, J.; Li, M.; Wang, D.; Chu, B.; Zhang, S.; Xu, Q.; Wang, K. Room Temperature Synthesis and Pressure-Induced Optical Properties of Lead-Free 2D $Cs_3Bi_2I_6Cl_3$ Perovskite Nanocrystals. *J. Mater. Chem. A* **2023**, *11* (36), 19427−19434.
(29) Liu, M.; Ali-Löytty, H.; Hiltunen, A.; Sarlin, E.; Qudsia, S.; Smått, J.-H.; Valden, M.; Vivo, P. Manganese Doping Promotes the Synthesis of Bismuth-Based Perovskite Nanocrystals While Tuning Their Band Structures. *Small* **2021**, *17* (19), 2100101.
(30) Ali, R. F.; Andreu, I.; Gates, B. D. Green Solvent Assisted Synthesis of Cesium Bismuth Halide Perovskite Nanocrystals and the Influences of Slow and Fast Anion Exchange Rates. *Nanoscale Adv.* **2019**, *1* (11), 4442−4449.
(31) Hoye, R. L. Z.; Eyre, L.; Wei, F.; Brivio, F.; Sadhanala, A.; Sun, S.; Li, W.; Zhang, K. H. L.; MacManus-Driscoll, J. L.; Bristowe, P. D.; Friend, R. H.; Cheetham, A. K.; Deschler, F. Fundamental Carrier Lifetime Exceeding 1 Ms in $Cs_2AgBiBr_6$ Double Perovskite. *Adv. Mater. Interfaces* **2018**, *5* (15), 1800464.
(32) Saparov, B.; Hong, F.; Sun, J.-P.; Duan, H.-S.; Meng, W.; Cameron, S.; Hill, I. G.; Yan, Y.; Mitzi, D. B. Thin-Film Preparation and Characterization of $Cs_3Sb_2I_9$: A Lead-Free Layered Perovskite Semiconductor. *Chem. Mater.* **2015**, *27* (16), 5622−5632.
(33) Grandhi, G. K.; Hardy, D.; Krishnaiah, M.; Vargas, B.; Al-Anesi, B.; Suryawanshi, M. P.; Solis-Ibarra, D.; Gao, F.; Hoye, R. L. Z.; Vivo, P. Wide-Bandgap Perovskite-Inspired Materials: Defect-Driven Challenges for High-Performance Optoelectronics (Adv. Funct. Mater. 50/2024). *Adv. Funct. Mater.* **2024**, *34* (50), 2470295.
(34) Le Corre, V. M. Space-Charge-Limited Current Measurements: A Problematic Technique for Metal Halide Perovskites. *J. Phys. Chem. Lett.* **2024**, *15* (39), 10001−10008.
(35) Wang, B.; Li, N.; Yang, L.; Dall'Agnese, C.; Jena, A. K.; Sasaki, S.; Miyasaka, T.; Tamiaki, H.; Wang, X.-F. Chlorophyll Derivative-Sensitized TiO_2 Electron Transport Layer for Record Efficiency of

https://doi.org/10.1021/acsomega.6c01559
ACS Omega 2026, 11, 30219−30235

$Cs_2AgBiBr_6$ Double Perovskite Solar Cells. *J. Am. Chem. Soc.* **2021**, *143* (5), 2207−2211.
(36) Bonomi, S.; Marongiu, D.; Sestu, N.; Saba, M.; Patrini, M.; Bongiovanni, G.; Malavasi, L. Novel Physical Vapor Deposition Approach to Hybrid Perovskites: Growth of $MAPbI_3$ Thin Films by RF-Magnetron Sputtering. *Sci. Rep.* **2018**, *8* (1), 15388.
(37) Hwang, J.-K.; Jeong, S.-H.; Kim, D.; Lee, H.-S.; Kang, Y. A Review on Dry Deposition Techniques: Pathways to Enhanced Perovskite Solar Cells. *Energies* **2023**, *16* (16), 5977.
(38) Konstantakou, M.; Perganti, D.; Falaras, P.; Stergiopoulos, T. Anti-Solvent Crystallization Strategies for Highly Efficient Perovskite Solar Cells. *Crystals* **2017**, *7* (10), 291.
(39) Yan, J.; Li, H.; Aldamasy, M. H.; Frasca, C.; Abate, A.; Zhao, K.; Hu, Y. Advances in the Synthesis of Halide Perovskite Single Crystals for Optoelectronic Applications. *Chem. Mater.* **2023**, *35* (7), 2683−2712.

https://doi.org/10.1021/acsomega.6c01559
ACS Omega 2026, 11, 30219−30235